Anomalous Elastic Response of a 3D Anti - Tetrachiral Metamaterial

Chang Quan Lai[1*], Kalaimani Markandan[1], Zhen Lu[2]

[1]*Temasek Laboratories, Nanyang Technological University, 50 Nanyang Drive, Singapore 637553*

[2]*SLM Solutions Singapore Pte Ltd, 25 International Business Park, German Centre, Singapore 609916*

[*] cqlai@ntu.edu.sg

Keywords:

Size Effect, Edge Effect, Chiral, Auxetic, Rotation-Dominated, Nonlinear, Metamaterial

Abstract

The elastic modulus and Poisson's ratio of a 3D anti-tetrachiral (3ATC) metamaterial design was investigated using an exact analytical model, finite element simulations and experiments on additively manufactured Ti6Al4V lattices. The 3ATC structure was found to undergo a unique symmetric-to-asymmetric transition as the number of unit cells in the lattice decreases, an observation that has not been reported to date. A reduced lattice size also increases the influence of shear forces introduced by the fixed boundary conditions, which can lead to a higher elastic modulus in certain orientations and reduce it in others. These shear forces also drive the joints in small lattices into an out-of-plane rotation that causes the Poisson's ratio of such structures to range from -1.2 to 1 for different relative densities, in contrast to a constant value of -0.5 for bulk 3ATC lattices that do not undergo this joint twisting. Our results also strongly indicate that the 3ATC structure belongs to a new 'rotation-dominated' geometric class in the Ashby framework for cellular materials, in addition to the well-established bending- and stretch- dominated topologies. The main contributor of strain for this class of materials is

rigid joint rotation, with novel, distinctive traits such as a nonlinear elastic stress-strain response and multiple *relative modulus* vs. *relative density* relationships. For the 3ATC structure, one of these relations is linear, similar to stretch-dominated structures, while the other is disjointed and does not follow the power law, which is atypical of a cellular material.

1. Introduction

Chiral lattices are structures with a repeating unit cell or sub-unit cell that cannot be superimposed onto its own mirror image through rotation or translation [1,2]. This chirality implies that the cells have a right-handed or left-handed spin directionality. As a result, under elastic mechanical loading, a chiral design would tend to deform through rotation about rigid joints, which also results in the buckling/ bending of any attached trusses [3–5].

This joint rotation can lead to auxetic behavior (*i.e.* negative Poisson's ratio) [6–8], which imbues chiral structures with desirable properties such as enhanced indentation resistance, fracture toughness and transverse shear modulus [2,9,10], as well as improved energy absorption efficiency [4,11,12] and acoustic mitigation characteristics [13–15]. Chiral lattices are also known to exhibit negative thermal expansion coefficients when bi-material trusses are used [2,16]. Moreover, the large change in nominal volume achievable with chiral designs makes them useful for retractable stents employed in cardiovascular surgeries [17], protective fabrics [18] and morphing airfoils [19–22].

In recent years, there has been a proliferation of studies on chiral lattices ranging from theoretical modelling to deployment in engineering applications [23–36]. The designs can generally be classified as chiral (*i.e.* net chirality in lattice $\neq 0$ *e.g.* tessellation of a single chiral unit cell), anti-chiral (*i.e.* net chirality in lattice = 0, as chiral sub-unit cells are joined with their mirror images that cancel out their chirality) and meta-chiral (made up of more than 1 type of chiral unit cell) [2]. However, the interest in chiral lattices, thus far, is mainly focused on 2D

structures, which are easier to fabricate and analyze [11,37–40]. For practical applications in lightweight vehicular parts and sports equipment, however, 3D structures can be more advantageous, as they provide functionality in all three dimensions, as well as higher levels of porosity [4,12,41,42]. This was demonstrated in a recent study, where 3D anti-tetrachiral (3ATC) lattices subjected to dynamic loading exhibited impact absorption efficiencies that were amongst the best in the literature [4].

Despite the promising results, however, the mechanical properties of the 3ATC auxetic metamaterial design has yet to be studied parametrically with respect to its various geometric parameters, lattice size and boundary conditions. For this reason, the effect of the number of unit cells on the elastic modulus and Poisson's ratio of the 3ATC lattice under clamped-clamped boundary conditions is investigated presently, with an analytical model, numerical computations and experiments. The relative density of the 3ATC structure will be comprehensively varied using all the available independent geometric parameters.

2. Design

The 3D anti-tetrachiral (3ATC) design studied here has been described previously [4,5] (Fig. 1a), and belongs to a family of similar auxetic structures [43–46]. The geometry is basically made up of a chiral sub-unit cell which has plane projections equivalent to the 2D anti-tetrachiral structure [37] (Fig. 1b). Under uniaxial loading, the central rigid joint, which is a cube here, rotates and bends the attached trusses (Fig. 1c and 1d). Each sub-unit cell is linked adjacently to its mirror image, so that 8 sub-unit cells form a single unit cell with no net chirality. In other words, when the unit cell is loaded uniaxially, the central joints of the sub-unit cells rotate in opposite directions, cancelling each other out, and as a result, the unit cell exhibits no net rotation (Fig. 1e). This unit cell can be tessellated cubically to form a larger lattice (Fig. 1a). The smallest lattice size studied here consists of 1 x 1 x 1 unit cell (*i.e.* unit-cell lattice).

The dimensions of the sub-unit cell are given in Fig. 1a. The anti-tetrachiral design can be completely described by 4 geometrical parameters, e (positional eccentricity of opposite trusses), a (width of central joint), L (length of truss) and w (width of truss) or 3 independent dimensionless parameters, w/a, L/a and e/a. The relative density, ρ/ρ_s, of the lattice, which is the ratio of the lattice, ρ, to the constitutive material, ρ_s, is dependent on only 2 of the parameters, L/a and w/a. The elastic response of the lattice, on the other hand, will depend on all 3 (see next Section). This stands in contrast to previous analyses on foams and lattices, where mechanical properties and relative density are both only dependent on 1 independent parameter, w/L, as it is generally assumed that $a = w$. This is not possible with the 3ATC design, however, as it would reduce the geometry to a non-chiral, simple cubic structure (*i.e.* $e = 0$).

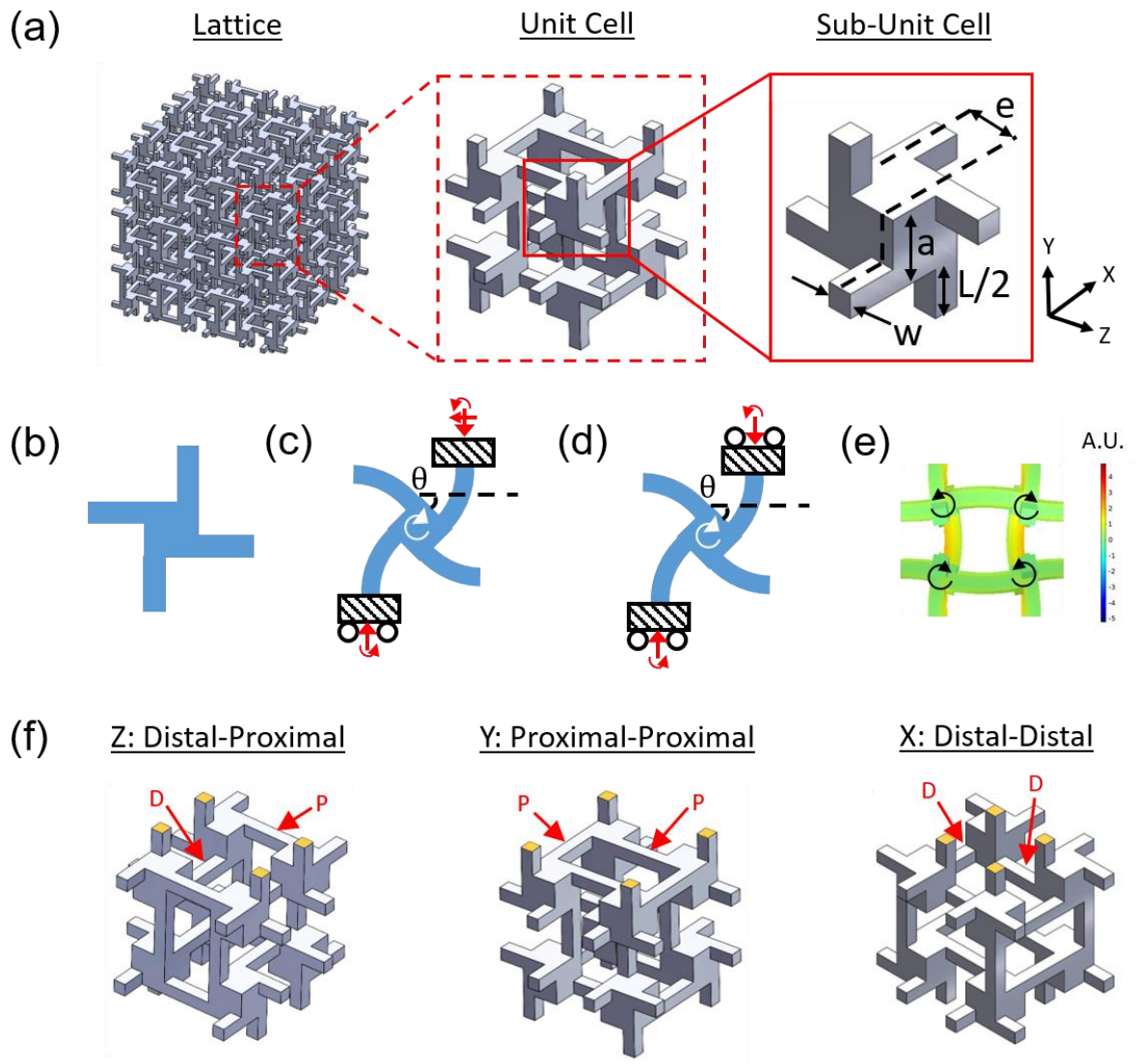

Figure 1: (a) Schematic diagrams showing a 3D anti-tetrachiral lattice, its unit cell and its sub-unit cell. (b) Projection of the undeformed sub-unit onto a plane. Free body diagrams showing the boundary conditions for (c) a sub-unit cell with the top vertical truss connected to the clamped/ fixed boundary and (d) a sub-unit cell in the bulk. (e) Finite element simulation showing the deformation of a unit cell. Note that the rotations of the sub-unit cells cancel each other out so that the overall unit cell is not chiral. (f) Different orientations of the unit cell when the clamped-clamped conditions are applied in different axes, following the coordinate system laid out in (a). The fixed surfaces are highlighted in yellow. D and P refer to lateral trusses that are distal and proximal to the fixed boundary surfaces respectively.

Focusing on a single unit cell, it can be noted that the geometry is not symmetric about the *X*, *Y* and *Z* axes (Fig. 1f). The key difference lies in the distance between the horizontal load-carrying trusses and the clamped boundaries (surfaces highlighted in yellow in Fig. 1f). Using the coordinates set forth in Fig. 1a, if the clamped-clamped boundary conditions are

applied in the Z-axis, for every sub-unit cell, there would be 1 horizontal, load-bearing truss that is proximal to the boundary surfaces (indicated by **P** in Fig. 1f) and 1 such truss that is distal to the same boundaries (indicated by **D** in Fig. 1f). If the boundaries are applied in the *Y*-axis, it would result in 2 horizontal trusses that are proximal to the boundary surfaces. If the same conditions are applied along the *X*-axis, it would result in 2 distal trusses instead.

However, if the unit cells are tessellated to form a larger lattice, then every sub-unit cell in the bulk will now have 2 proximal and 2 distal load-bearing trusses (Fig. 1a). As the lattice gets larger, the number of symmetric bulk sub-unit cells will increasingly outweigh the number of asymmetric edge and corner sub-unit cells, so that the geometric asymmetry eventually disappears. Therefore, based on this qualitative assessment, the 3ATC geometry is expected to exhibit a size-dependent asymmetric-to-symmetric mechanical property transition, which will be further examined in detail in the "Results" and "Discussion" sections.

3. Methods

3.1. Simulations

3D anti-tetrachiral (3ATC) lattices were designed using SOLIDWORKS (Dassault Systemes). The details of the geometries investigated for this study can be found in Table A1 (Appendix).

Finite element simulations were conducted using COMSOL multiphysics modeling software (COMSOL Inc.). The geometries were imported from SOLIDWORKS and the simulations were carried out using the "Stationary" solver under the "Solid Mechanics" module, with "geometric nonlinearity" considerations included. The number of tetrahedral elements in each geometric mesh can range from ~ 20,000 for a single unit-cell lattice to ~ 500,000 for a 3 x 3 x 3 lattice.

Each lattice was compressed to at least 1% strain in 1/20 steps. The lattice stress was obtained by dividing the total normal force acting on the clamped boundary surfaces with the nominal lattice area. To compute the modulus, E, for strain $\rightarrow$ 0, the engineering stress-strain response of the structures was plotted and fitted with a sixth order polynomial (see Section 5.1). The transverse strain can be obtained by dividing the total displacement of the outermost horizontal trusses with the nominal width of the lattice. This, when divided by the strain of the lattice in the loading axis, then gives the lattice Poisson's ratio, ν.

3.2. Fabrication and Characterization

3ATC lattices were additively manufactured from Ti6Al4V powder (diameter = 20 – 63 μm) using selective laser melting (SLM® 280 2.0, SLM Solutions Group AG) in Argon atmosphere (0.00% O_2 monitored) with a layer thickness of 30 μm. The 3D printed structures showed good fidelity to the designs, with less than 0.5% deviation in dimensions. Experimental quasistatic stress-strain curves of the lattices were obtained at a strain rate of 0.01/s using

Shimadzu AG-X with a 100 kN load cell. The porosity, obtained through mass density measurements, and elastic modulus, E_s, of the 3D printed Ti6Al4V material were determined to be ~ 20% and ~ 60 GPa respectively, which are in line with results of previous reports [47,48].

4. Analytical Model

In this section, the exact expressions (*i.e.* without fitting parameters) for the elastic response of the 3D anti-tetrachiral (3ATC) lattices under clamped-clamped uniaxial loading will be derived for the 2 extremes in lattice size, unit-cell and infinite. The analysis makes use of the Euler-Bernoulli beam model and focuses on the small force/ strain regime. Key equations are highlighted with an asterisk and summarized in Table 1. The derivation for an anisotropic infinite 3ATC lattice had been presented previously [4], so the section on the bulk lattice here will simply be a brief recap, with appropriate simplifications made for the cubic symmetric (*i.e.* symmetrical about the *X*, *Y* and *Z* axes) of the 3ATC design studied here.

Table 1: Key equations for the properties of different lattice geometries.

Geometry		Modulus	Poisson's Ratio
Position of Lateral Load-Bearing Trusses with Respect to the Boundary Surfaces	**Position of Each Lateral Load-Bearing Truss with Respect to the Boundary Truss**		
Distal - Distal	Same Plane	(62), (64)-(67)	(70)
	Different Plane	(63), (64)-(67)	(71)
Proximal - Proximal	Same Plane	(72), (64)-(67)	(90)
	Different Plane	(73), (64)-(67)	(91)
Distal - Proximal	Proximal (Different Plane)	(13), (78), (79), (64)-(67)	(90)
	Distal (Different Plane)	(13), (80), (81), (64)-(67)	(91)
Bulk		(94), (64)-(67)	(96)

4.1. Distal-Distal (*D-D*) Arrangement

4.1.1. Truss I

Consider the free body diagram of Truss I, which has one end fixed to the boundary, in Fig. 2a. Equilibrating the forces yields,

$$E_s I v_I'''[y] + F v_I'[y] = -V_x \tag{1}$$

where *f*[*y*] refers to a function dependent on *y*. v_I refers to the deflection of Truss I, E_s refers to the Young's modulus of the material and *I* refers to the second moment of area, which is

$$I = \frac{1}{12} w^4 \tag{2}$$

for a truss with a square cross-section and width of *w*.

Taking moments about the point of origin (red cross in Fig. 2a), under static equilibrium,

$$E_s I v_I''[y] = \frac{\tau_x L}{2} + F v_I\left[\frac{L}{2}\right] - M_I - F v_I[y] - V_x y \tag{3}$$

Noting that Truss I is subjected to the boundary conditions of

$$v_I[0] = 0 \tag{4}$$

and

$$v_I'[0] = 0 \tag{5}$$

the deflection of Truss I can be solved using Eq. (1) and Eq. (3) as

$$v_I[y] = A_1 \cos(ky) + A_2 \sin(ky) + A_3 y + A_4 \tag{6}$$

where

$$A_1 = \frac{M_I}{F\cos\left(\frac{kL}{2}\right)} - \frac{V_x}{kF} tan\left(\frac{kL}{2}\right) \tag{7}$$

$$A_2 = \frac{V_x}{kF} \tag{8}$$

$$A_3 = -\frac{V_x}{F} \tag{9}$$

$$A_4 = -A_1 = -\frac{M_I}{F\cos\left(\frac{kL}{2}\right)} + \frac{V_x}{kF} tan\left(\frac{kL}{2}\right) \quad . \tag{10}$$

and

$$k = \sqrt{\frac{F}{E_s I}} \tag{11}$$

Therefore, the deflection, $v_I[L/2]$, and slope, $v_I'[L/2]$, for Truss I at the "free" end, where it joins with the central cube, can be written as

$$v_I\left[\frac{L}{2}\right] = \frac{M_I}{F}\left\{1 - \frac{1}{cos\left(\frac{kL}{2}\right)}\right\} + \frac{V_x}{kF}\left\{tan\left(\frac{kL}{2}\right) - \frac{kL}{2}\right\} \tag{12}$$

and

$$v_I'\left[\frac{L}{2}\right] = \theta = -\frac{M_I k}{F} tan\left(\frac{kL}{2}\right) + \frac{V_x}{F}\left\{\frac{1}{cos\left(\frac{kL}{2}\right)} - 1\right\} \tag{13}*$$

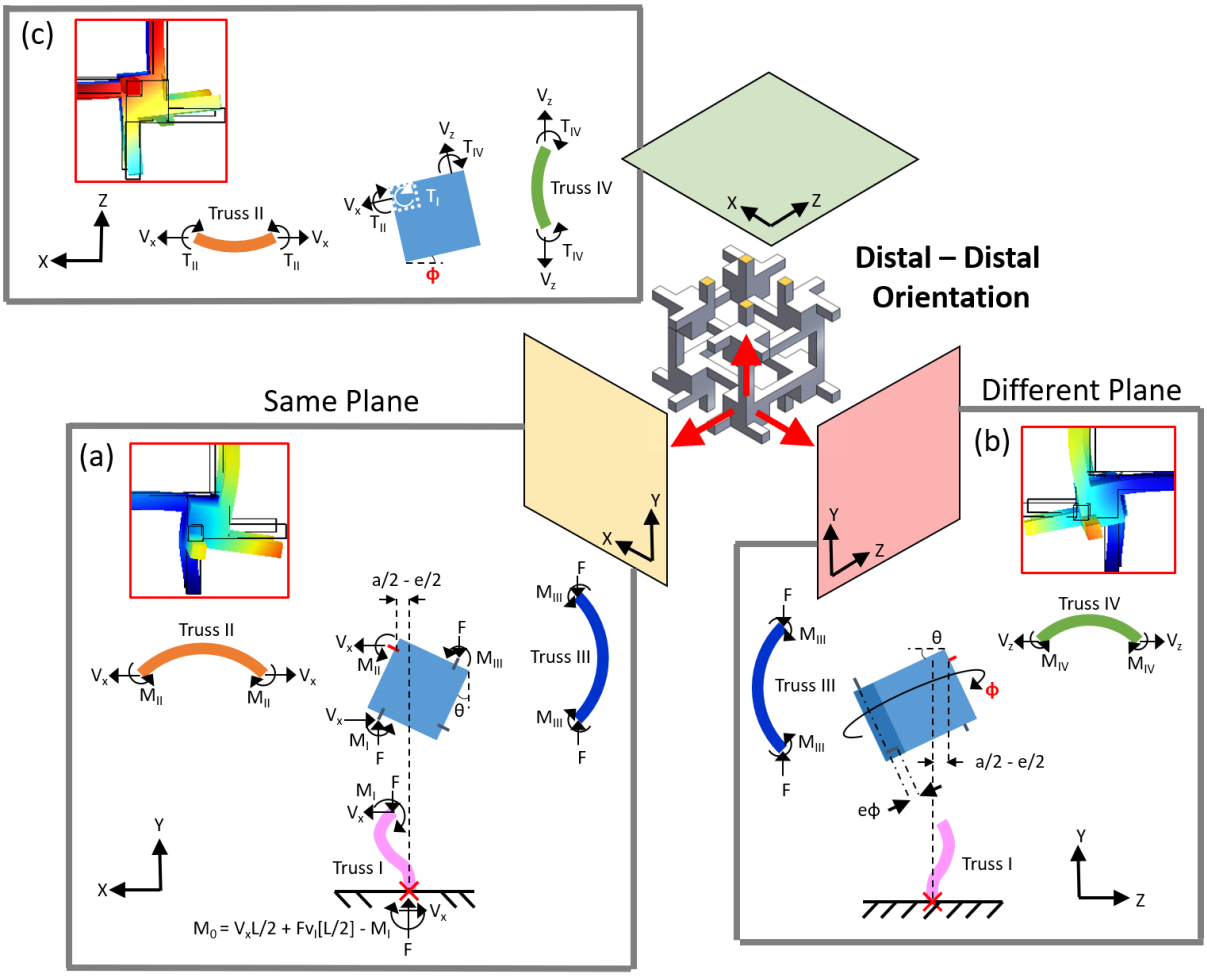

Figure 2: Free-body diagrams of the anti-tetrachiral unit-cell lattice, oriented in such a way that both load-bearing lateral trusses are distal to the clamped boundaries. The clamped boundaries are highlighted in yellow. The clamping is symmetrical, so the ends of the bottom-most vertical trusses are clamped as well. There are no constraints on the lateral sides of the lattice. The uniaxial load is applied vertically on the clamped surfaces. Because of symmetry, only the free-body diagrams for the bottom sub-unit cell (centre of the 3 red arrows) in different planes are shown. For simplicity, only load-bearing trusses are depicted. The point of origin for Truss I is marked by a red cross. The dashes at the perimeter of the central cubic joint indicate the positions where the trusses join with the cube. The red dash indicates the pivot of rotation i.e. the horizontal position of this point, at the end of the load-bearing lateral truss, is fixed. (a) Transverse Plane 1: The boundary truss, Truss I, is in the same plane as the load-bearing lateral truss, Truss II. (b) Transverse Plane 2: Truss I and the load-bearing lateral truss, Truss IV, are

in parallel planes offset by a distance of e. (c) Loading Plane: Top view showing the joint and the 2 lateral trusses, II and IV. θ is the in-plane rotation and may be different in (a) and (b). ϕ is the out-of-plane rotation that is the same in all planes (not shown in (a) as it does not impose additional horizontal constraints that will influence θ). (Insets) Images from finite element simulations illustrating the deformation of the sub-unit cell in the respective planes.

4.1.2. Truss II

For the laterally positioned Truss II (Fig. 1a), equilibrium of shear forces dictates that

$$E_s I v_{II}''''[x] - F v_{II}''[x] = 0 \tag{14}$$

while the equilibrium of moments means

$$E_s I v_{II}''[0] = -M_{II} \tag{15}$$

Note that the point of origin for Truss II is located at its ends. Due to symmetry, either end can be taken as the point of origin. Its deformation is subjected to the constraints,

$$v_{II}[0] = 0 \tag{16}$$

$$v_{II}[L] = 0 \tag{17}$$

$$v_{II}'\left[\frac{L}{2}\right] = 0 \tag{18}$$

Solving Eq. (14) – (18) gives the deflection of Truss II, v_{II}, as

$$v_{II}[x] = B_1 \exp(\alpha x) + B_2 \exp(-\alpha x) + B_3 x + B_4 \tag{19}$$

where $$\alpha = \sqrt{\frac{V_x}{E_s I}} \tag{20}$$

Since V_x, and by extension, α, is small, the following substitutions,

$$\exp(\alpha x) \approx 1 + \alpha x + \frac{1}{2}\alpha^2 x^2 + \frac{1}{6}\alpha^3 x^3 \tag{21}$$

and $$\exp(-\alpha x) \approx 1 - \alpha x + \frac{1}{2}\alpha^2 x^2 - \frac{1}{6}\alpha^3 x^3 \tag{22}$$

can be used based on the Taylor series. The constants in Eq. (19) can then be found as

$$B_1 = B_2 = -\frac{M_{II}}{2V_x} \tag{23}$$

$$B_3 = \frac{M_{II} L}{2E_s I} \tag{24}$$

$$B_4 = \frac{M_{II}}{V_x} \tag{25}$$

and the slope at the end of Truss II can be expressed as

$$v_{II}'[0] = B_3 = \frac{M_{II}L}{2E_sI} \tag{26}$$

4.1.3. <u>Truss III</u>

For Truss III, its horizontal position is not as constrained as that of Truss I and Truss II and therefore, it is not expected to take significant shear loads at its ends. Based on the resultant free body diagram, the equilibrium of forces yields

$$E_sIv_{III}''''[y] + Fv_{III}''[y] = 0 \tag{27}$$

and the equilibrium of moments yields

$$E_sIv_{III}''[0] = M_{III} \tag{28}$$

Truss III is also subjected to the constraints of

$$v_{III}[0] = 0 \tag{29}$$

$$v_{III}[L] = 0 \tag{30}$$

$$v_{III}'\left[\frac{L}{2}\right] = 0 \tag{31}$$

where, like Truss II, the point of origin is located at either end of the truss.

The solution for the deflection of Truss III, v_{III}, is then

$$v_{III}[y] = C_1\cos(ky) + C_2\sin(ky) + C_3y + C_4 \tag{32}$$

where

$$C_1 = -\frac{M_{III}}{F} \tag{33}$$

$$C_2 = -\frac{M_{III}}{F}tan\left(\frac{kL}{2}\right) \tag{34}$$

$$C_3 = 0 \tag{35}$$

$$C_4 = \frac{M_{III}}{F} \tag{36}$$

and the slope at its ends is

$$v_{III}'[0] = -\frac{M_{III}k}{F} tan\left(\frac{kL}{2}\right) \tag{37}$$

4.1.4. Constraint on the End Slopes of Trusses I, II and III

Based on the local axes chosen, the slopes at the ends of Trusses I and III are negative while that for Truss I is positive. The magnitude of each slope, θ, however, should be the same as all the trusses are all connected to the central rigid joint at a fixed angle of 90°. Note that θ is also the rotation of the central cube in the *X*-*Y* plane. Expressing this constraint mathematically gives

$$\theta = v_I'\left[\frac{L}{2}\right] = v_{III}'[0] = -v_{II}'[0] \tag{38}$$

which allows M_{II} and M_{III} to be expressed as functions of M_I and V_x,

$$M_{II} = \left\{\frac{2}{kL} tan\left(\frac{kL}{2}\right)\right\} M_I - \left\{\frac{2}{k^2 L}\left(\frac{1}{cos\left(\frac{kL}{2}\right)} - 1\right)\right\} V_x \tag{39}$$

$$M_{III} = M_I - \left\{\frac{1-cos\left(\frac{kL}{2}\right)}{ksin\left(\frac{kL}{2}\right)}\right\} V_x \tag{40}$$

To get independent expressions of M_I and V_x, 2 additional constraints will be required, and they will be obtained in the following by considering the equilibrium of moments about the rigid joint, as well as the relationship between the horizontal deflection of Truss I and the horizontal displacements brought about by the joint rotations.

4.1.5. Equilibrium of Moments about the Rigid Joint

Taking equilibrium of moments about the central cube (in blue in Fig. 2a),

$$M_I + M_{II} + M_{III} + \left(\frac{a}{2} + \frac{e}{2}\right) V_x = Fe \tag{41}$$

4.1.6. <u>Same Plane</u>

As the lattice deforms, we note that the length of Truss II should remain very much the same throughout *i.e.* the ends of Truss II should remain at the same horizontal coordinates before and after deformation. Note that the vertical position of the ends, however, are not fixed. Therefore, when the central cube rotates, it pivots about the end of the lateral truss (indicated by a red line on the cube). The implication of this constraint is that the lateral deflection of Truss I must be counter to and equivalent to any lateral displacements caused by the rotation of the cube.

In the *X*-*Y* plane, the lateral truss, Truss II, is in the same plane as the fixed boundary strut, Truss I. Therefore, the lateral displacement of Truss I at its end, $v_I[L/2]$, must equal the lateral displacement caused by the rotation of cube in the *X*-*Y* plane, θ. This constraint can be expressed as

$$\left\{\left(\frac{a}{2}-\frac{e}{2}\right)-\sqrt{\frac{a^2+e^2}{2}}sin(\beta-\theta)\right\}+v_I\left[\frac{L}{2}\right]=0 \tag{42}$$

where

$$tan(\beta)=\frac{a+e}{a-e} \tag{43}$$

Since θ (= $v_I'[L/2]$) is small and from Eq. (38), Eq. (42) can be re-written as

$$\left(\frac{a}{2}+\frac{e}{2}\right)\left(v_I'\left[\frac{L}{2}\right]\right)+v_I\left[\frac{L}{2}\right]=0 \tag{44}$$

Note that the deflection, $v_I[L/2]$, is positive and the slope, $v_I'[L/2]$, is negative here. Substituting the expressions for M_{II} and M_{III} in Eq. (39) and (40) into Eq. (41) and substituting the expressions for $v_I[L/2]$ and $v_I'[L/2]$ in Eq. (12) and (13) into Eq. (44) will yield 2 equations that can then be solved simultaneously to give

$$V_x=\frac{Q_D}{R_D}M_I \tag{45}$$

$$M_I = \frac{Fe}{2+S+\frac{Q_D}{R_D}\left(\frac{a}{2}+\frac{e}{2}+U+N\right)} \tag{46}$$

where

$$Q_D = \left(\frac{a}{2}+\frac{e}{2}\right) k tan\left(\frac{kL}{2}\right) + \frac{1}{cos\left(\frac{kL}{2}\right)} - 1 \tag{47}$$

$$R_D = \left(\frac{a}{2}+\frac{e}{2}\right)\left(\frac{1}{cos\left(\frac{kL}{2}\right)} - 1\right) + \frac{1}{k}\left(tan\left(\frac{kL}{2}\right) - \frac{kL}{2}\right) \tag{48}$$

$$S = \frac{2}{kL} tan\left(\frac{kL}{2}\right) \tag{49}$$

$$U = -\frac{2}{k^2 L}\left(\frac{1}{cos\left(\frac{kL}{2}\right)} - 1\right) \tag{50}$$

$$N = -\frac{1-cos\left(\frac{kL}{2}\right)}{ksin\left(\frac{kL}{2}\right)} \tag{51}$$

4.1.7. <u>Different Plane</u>

Upon closer inspection, it can be observed that the geometry of the sub-unit cell in the *X-Y* plane is not the same as that in the *Y-Z* plane. Here, Truss I, and the lateral truss, Truss IV, are in parallel planes offset by a distance of *e* (Fig. 2b). Truss IV is distinguished from Truss II to highlight that it is a different lateral truss, in another plane. Because of this offset, there will be an out-of-plane rotation of the cube in the *X-Z* plane, ϕ, which adds a lateral displacement of approximately $e\phi$ to Eq. (44).

Examining the free-body diagrams in Fig. 2c it can be seen that the slopes at the ends of Truss II and IV in the *X-Z* plane, $u_{II}'[0]$ and $u_{IV}'[0]$ respectively, follow the expression in Eq. (26). Again, because these trusses are connected to the same rigid joint, their slopes must be equal to ϕ *i.e.*

$$u_{II}'[0] = \frac{T_{II}L}{2E_sI} = u_{IV}'[0] = \frac{T_{IV}L}{2E_sI} = \phi \tag{52}$$

From Eq. (52), it is clear that $T_{II} = T_{IV}$.

For the torques and moments acting on the central cube to be in equilibrium in the *X*-*Z* plane (Fig. 2c), the torque acting on Truss I, T_I, can be expressed as

$$T_I = eV_z - T_{II} - T_{IV} = eV_z - 2T_{II} \tag{53}$$

Therefore, the angle of twist for Truss I, which is the same as the rotation of the cube in the *X*-*Z* plane, ϕ, is

$$\phi = \frac{T_I \frac{L}{2}}{JG_s} \tag{54}$$

where polar moment of inertia, *J*, and shear modulus, G_s, can be written as

$$J = \frac{1}{6}w^4 \tag{55}$$

$$G_s = \frac{E_s}{2(1+\upsilon_s)} \tag{56}$$

ν_s and E_s refers to the constituent material's Poisson's ratio and modulus respectively. Substituting Eq. (53) - (56) into Eq. (52) yields

$$T_{II} = \frac{1+\upsilon_s}{3+2\upsilon_s} eV_z \tag{57}$$

$$\phi = \frac{eL}{2E_s I}\left(\frac{1+\upsilon_s}{3+2\upsilon_s}\right) V_z \tag{58}*$$

Having found the rotation of the cube in the *X*-*Z* plane, ϕ, we consider the conservation of Truss IV's length again, noting that the rotation of the cube by ϕ in the *X*-*Z* plane causes an additional lateral displacement of approximately $e\phi$ in the *Y*-*Z* plane. Including this additional component in Eq. (44) gives

$$\left(\frac{a}{2} + \frac{e}{2}\right)\left(\upsilon_I{}'\left[\frac{L}{2}\right]\right) + \upsilon_I\left[\frac{L}{2}\right] + e|\phi| = 0 \tag{59}$$

Note that the deflection ($v_I[L/2]$) is positive and the slope ($v_I'[L/2]$) is negative here. Substituting the expressions for M_{II} and M_{III} in Eq. (39) and (40) into Eq. (41) and substituting the expressions for $v_I[L/2]$ and $v_I'[L/2]$ in Eq. (12) and (13) into Eq. (59) will yield 2 equations that can then be solved simultaneously to give

$$V_z = \frac{Q_D}{R_D + \frac{e^2 k^2 L}{2}\left(\frac{1+\upsilon_S}{3+2\upsilon_S}\right)} M_I \tag{60}$$

$$M_I = \frac{Fe}{2+S+\frac{Q_D}{R_D + \frac{e^2 k^2 L}{2}\left(\frac{1+\upsilon_S}{3+2\upsilon_S}\right)}\left(\frac{a}{2}+\frac{e}{2}+U+N\right)} \tag{61}$$

4.1.8. Stress-Strain Relationship

For the distal-distal arrangement, the geometry of the sub-unit cell is such that in one plane, the fixed truss and the lateral truss will be in the same plane, while in the other plane, the fixed truss and the lateral truss will be offset by a distance of *e*. Denoting the first case as *sp* (same plane) and the latter case as *dp* (different plane), the rotation of the central cube for each case can be found using the expression for $v_I'[L/2]$ in Eq. (13), by substituting in the case-specific M_I, V_x and V_z expressions described in Eq. (45), (46), (60) and (61), which leads to

$$\theta_{sp} = \frac{e}{2+S+\frac{Q_D}{R_D}\left(\frac{a}{2}+\frac{e}{2}+U+N\right)}\left\{-ktan\left(\frac{kL}{2}\right) + \frac{Q_D}{R_D}\left\{\frac{1}{cos\left(\frac{kL}{2}\right)} - 1\right\}\right\} \tag{62}*$$

$$\theta_{dp} = \frac{e}{2+S+\frac{Q_D}{R_D + \frac{e^2 k^2 L}{2}\left(\frac{1+\upsilon_S}{3+2\upsilon_S}\right)}\left(\frac{a}{2}+\frac{e}{2}+U+N\right)}\left\{-ktan\left(\frac{kL}{2}\right) + \frac{Q_D}{R_D + \frac{e^2 k^2 L}{2}\left(\frac{1+\upsilon_S}{3+2\upsilon_S}\right)}\left\{\frac{1}{cos\left(\frac{kL}{2}\right)} - 1\right\}\right\} \tag{63}*$$

Note that *k* is a function of the force, *F* (see Eq. (11)), from which the stress on the lattice can be calculated. The shortening of the lattice height due to the rotation of the central cube, Δ_r, is then

$$\Delta_r = e\left(|\theta_{sp}| + |\theta_{dp}|\right) \tag{64}$$

The displacement due to compression, Δ_c, and that due to indentation of the truss into rigid joint [49], Δ_i, can be expressed as

$$\Delta_c = \frac{F}{E_S}\left(\frac{L}{w^2} + \frac{1}{a}\right) \tag{65}$$

$$\Delta_i = \frac{2F(1-\upsilon_S)}{4G_S w} \tag{66}$$

Finally, the overall *compressive* strain, ε, is a summation of these displacements and can be expressed as

$$\varepsilon = \frac{\Delta_r+\Delta_c+\Delta_i}{L+a} \tag{67}*$$

4.1.9. Poisson's Ratio

For the ***D***–***D*** arrangement, the same-plane rotation, θ, draws in the lateral trusses while the out-of-plane rotation, ϕ, pushes them outwards. Therefore, the net transverse strain can be written as

$$\varepsilon_{T,sp} = -\frac{e(|\theta_{sp}|-|\phi|)}{L+a} \tag{68}$$

and

$$\varepsilon_{T,dp} = -\frac{e(|\theta_{dp}|-|\phi|)}{L+a} \tag{69}$$

for the "same plane" and "different plane" geometries. The corresponding Poisson's ratios for the lattice, ν_{sp} and ν_{dp}, will then be

$$\upsilon_{sp} = -\frac{\varepsilon_{T,sp}}{\varepsilon} = -\frac{e(|\theta_{sp}|-|\phi|)}{\Delta_r+\Delta_c+\Delta_i} \tag{70}*$$

and

$$\upsilon_{dp} = -\frac{\varepsilon_{T,dp}}{\varepsilon} = -\frac{e(|\theta_{dp}|-|\phi|)}{\Delta_r+\Delta_c+\Delta_i} \tag{71}*$$

4.2. Proximal-Proximal (*P*-*P*) Arrangement

Following the same analysis as Section 4.1 (see Appendix for details), the rotations of the cubic joint for the ***P-P*** orientation can be given by

$$\theta_{sp} = -\frac{e}{2+S+\frac{Q_P}{R_P}\left(\frac{a}{2}-\frac{e}{2}+U+N\right)}\left\{-ktan\left(\frac{kL}{2}\right)+\frac{Q_P}{R_P}\left\{\frac{1}{cos\left(\frac{kL}{2}\right)}-1\right\}\right\} \tag{72}*$$

$$\theta_{dp} = \frac{e}{2+S+\frac{Q_P}{R_P+\frac{e^2k^2L}{2}\left(\frac{1+\upsilon_S}{3+2\upsilon_S}\right)}\left(\frac{a}{2}-\frac{e}{2}+U+N\right)}\left\{-ktan\left(\frac{kL}{2}\right)+\frac{Q_P}{R_P+\frac{e^2k^2L}{2}\left(\frac{1+\upsilon_S}{3+2\upsilon_S}\right)}\left\{\frac{1}{cos\left(\frac{kL}{2}\right)}-1\right\}\right\} \tag{73}*$$

These rotations can then be used to establish the quantitative stress-strain relationship for the ***P-P*** case using Eq. (64) – (67).

4.2.6. Poisson's Ratio

Unlike the ***D***–***D*** arrangement, for the ***P-P*** arrangement, the same-plane rotation, θ, draws in the lateral trusses, while the out-of-plane rotation, ϕ, draws them even further in. Therefore, the net transverse strain can be written as

$$\varepsilon_{T,sp} = -\frac{e(|\theta_{sp}|+|\phi|)}{L+a} \tag{74}$$

and

$$\varepsilon_{T,dp} = -\frac{e(|\theta_{dp}|+|\phi|)}{L+a} \tag{75}$$

The corresponding Poisson's ratios for the lattice, ν_{sp} and ν_{dp}, will then be

$$\upsilon_{sp} = -\frac{\varepsilon_{T,sp}}{\varepsilon} = -\frac{e(|\theta_{sp}|+|\phi|)}{\Delta_r+\Delta_c+\Delta_i} \tag{76}*$$

and

$$\upsilon_{dp} = -\frac{\varepsilon_{T,dp}}{\varepsilon} = -\frac{e(|\theta_{dp}|+|\phi|)}{\Delta_r+\Delta_c+\Delta_i} \tag{77}*$$

4.3. Distal-Proximal (*D-P*) Arrangement

For the ***D-P*** orientation, the horizontal truss is distal along a transverse axis and proximal along the other transverse axis. In both cases, the fixed boundary truss, Truss I, is in a parallel plane, offset by a distance of *e*, with respect to the horizontal trusses (see Appendix). Once again, following a similar method of analysis as the preceding sections for the ***D-P*** orientation (see Appendix for details), we can obtain

$$V_D = \frac{H_B+H_C}{H_AH_C-H_BH_D}eF \tag{78}*$$

$$M_{I,D} = \frac{(R_PR_D+eF\xi R_D+eF\xi R_P)(H_B+H_C)-eF\xi Q_P(H_A+H_D)}{Q_D(R_P+eF\xi)(H_AH_C-H_BH_D)}eF \tag{79}*$$

$$V_P = \frac{Q_P(H_A+H_D)+eF\xi(H_B+H_C)}{(R_P+eF\xi)(H_AH_C-H_BH_D)}eF \tag{80}*$$

$$M_{I,P} = \frac{H_A+H_D}{H_A H_C - H_B H_D} eF \quad (81)^*$$

where

$$H_A = \frac{R_D}{Q_D} C_{D0} C_1' - \left(\frac{eF\xi}{R_P+eF\xi} - 1\right) C_{D1} \quad (82)$$

$$H_B = \frac{R_D}{Q_D} C_{D0} C_2' - \frac{C_{D1} Q_P}{R_P+eF\xi} \quad (83)$$

$$H_C = C_{P0} - \frac{C_{P1} Q_P}{R_P+eF\xi} \quad (84)$$

$$H_D = \left(\frac{eF\xi}{R_P+eF\xi} - 1\right) C_{P1} \quad (85)$$

and

$$C_1' = 1 + \frac{eF\xi}{R_D} - \frac{(eF\xi)^2}{R_D(R_P+eF\xi)} \quad (86)$$

$$C_2' = \frac{eF\xi Q_P}{R_D(R_P+eF\xi)} \quad (87)$$

Finally, by substituting Eq. (78) and (79), as well as Eq. (80) and (81), into Eq. (13), the rotation of the central cube in the plane with distal lateral truss, θ_D, and proximal truss, θ_P, can be found respectively. These rotations can then be substituted into Eq. (64) – (67) to obtain the stress-strain relationship for the ***D-P*** orientation.

4.3.5. <u>Poisson's Ratio</u>

Like the ***P-P*** arrangement, the θ rotation draws in the lateral trusses while the ϕ rotation draws them even further in. Therefore, the overall transverse strain can be written as

$$\varepsilon_{T,D} = -\frac{e(|\theta_D|+|\phi|)}{L+a} \quad (88)$$

and

$$\varepsilon_{T,P} = -\frac{e(|\theta_P|+|\phi|)}{L+a} \quad (89)$$

for the planes with the distal and proximal trusses respectively. The corresponding Poisson's ratios for the lattice, ν_D and ν_P, will then be

$$\upsilon_D = -\frac{\varepsilon_{T,D}}{\varepsilon} = -\frac{e(|\theta_D|+|\phi|)}{\Delta_r+\Delta_c+\Delta_i} \quad (90)^*$$

and $$\upsilon_P = -\frac{\varepsilon_{T,P}}{\varepsilon} = -\frac{e(|\theta_P|+|\phi|)}{\Delta_r+\Delta_c+\Delta_i} \quad (91)^*$$

4.3. Bulk Lattice

The mechanical response of a unit cell in an infinite 3D anti-tetrachiral lattice has already been discussed in detail previously [4], and it has 2 main differences compared with a unit-cell lattice. Firstly, it cannot withstand horizontal shear stresses, as it is not constrained by the edges to remain laterally stationary in the bulk (Fig. 1d). Secondly, the geometry of an infinite lattice has cubic symmetry (*i.e.* geometry is the same in the *X*-, *Y*- and *Z*-axes), with each sub-unit cell having 2 load-bearing distal lateral trusses and 2 load-bearing proximal lateral trusses. As a result of these differences, the rotation of the rigid joint under uniaxial stress is the same in both transverse planes and has been derived to be [4]

$$\theta = \theta_{T1} = \theta_{T2} = -\frac{M_{v0}}{F} k tan\left(\frac{kL}{2}\right) \quad (92)$$

where

$$M_{v0} = \frac{eLF^2}{4E_s I k tan\left(\frac{kL}{2}\right)+2FL} \quad (93)$$

The subscript *T1* and *T2* refer to the first and second transverse plane respectively.

The displacement due to the rotation of the central cube, Δ_r, is then

$$\Delta_r = e(\theta_{T1} + \theta_{T2}) = 2e\theta \quad (94)^*$$

Eq. (94) can then be substituted into Eq. (67) to find the overall strain, ε.

The transverse strains, ε_{T1} and ε_{T2} are only determined by the in-plane rotation, θ, since there is no out-of-plane rotation, ϕ, so that

$$\varepsilon_{T1} = \varepsilon_{T2} = -\frac{e|\theta|}{L+a} \quad (95)$$

and the Poisson's ratio for an infinite lattice can be written as

$$\upsilon = \upsilon_{T1} = \upsilon_{T2} = -\frac{\varepsilon_{T1}}{\varepsilon} = -\frac{e|\theta|}{\Delta_r+\Delta_c+\Delta_i} \quad (96)^*$$

4.4. Dependence on Material Parameters

In the limit of small loading force, F, the trigonometric expressions where k is the argument can be estimated using small angle approximations. It can then be observed that Δ_r, Δ_a and Δ_i, and therefore, ε, is proportional to F/E_s for all of the geometric configurations. Since lattice stress, σ, is given by

$$\sigma = \frac{F}{(L+a)^2} \tag{97}$$

and the lattice modulus, E, is given by

$$\mathrm{E} = \frac{\sigma}{\varepsilon} \tag{98}$$

therefore,

$$\mathrm{E} \propto E_s \tag{99}$$

Other than the material's native modulus, E_s, the lattice modulus, E, is also a function of the material's native Poisson's ratio, ν_s, for the unit-cell lattices. However, for common engineering materials with ν_s ranging between 0.3 and 0.5, the change in E was insignificant (< 1%). Therefore, if E is normalized by E_s, the lattice modulus of any 3ATC design becomes material independent and its value is determined solely by geometric parameters. As for the lattice Poisson's ratio, ν, it is naturally material independent and does not require normalization.

5. Results

5.1. Nonlinear Elastic Stress-Strain Response

Fig. 3a shows the stress-strain response of the unit-cell, 3D anti-tetrachiral (3ATC) lattices. The trends are nonlinear, but this is not a result of the size/ edge effect, as it is predicted and observed experimentally for unit cells in large lattices as well (Fig. 3b). In Fig. 3c and 5d, it can be observed that this nonlinearity extends to the lattice Poisson's ratios. The analytical model predicts the stress-strain relation and Poisson's ratio – strain trend reasonably well except at large strains, where the small load and small angle approximations fail. Note that experimental data could not be obtained for the Poisson's ratios, as the sub-unit cells undergo out-of-plane twisting in addition to in-plane deformations (see "Analytical Model"), and we have yet to develop a reliable experimental method to measure the position of the truss centroids, especially in the sensitive regime of $\varepsilon \sim 0.01$.

Both the elastic stress-strain and the Poisson's ratio-strain curves can be fitted with a polynomial trend up to the 6th order *i.e.*

$$\sigma = a_6\varepsilon^6 + a_5\varepsilon^5 + a_4\varepsilon^4 + a_3\varepsilon^3 + a_2\varepsilon^2 + a_1\varepsilon + a_0 \quad (100)$$

$$\nu = b_6\varepsilon^6 + b_5\varepsilon^5 + b_4\varepsilon^4 + b_3\varepsilon^3 + b_2\varepsilon^2 + b_1\varepsilon + b_0 \quad (101)$$

To simplify the following analysis, we shall focus on the elastic response in the limit of small strain (*i.e.* $\varepsilon \rightarrow 0$). Therefore, the elastic modulus, E, is dominated by and essentially equivalent to the coefficient, a_1, while $\nu \approx b_0$.

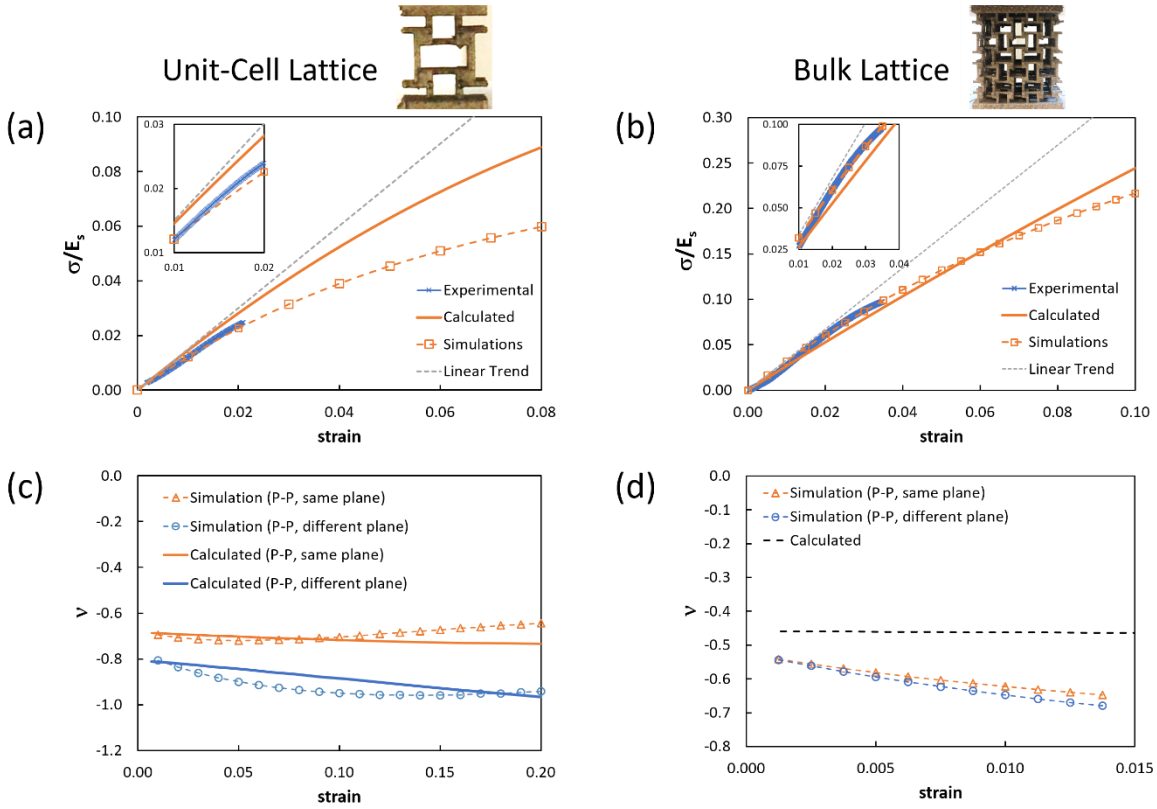

Figure 3: Engineering stress, σ, normalized by material modulus, E_s, vs engineering strain for the (a) unit-cell lattice (e/a = 2/3, L/a = 10/3, w/a = 1/3) (b) bulk lattice (e/a = 2/3, L/a = 4/3, w/a = 1/3). For theoretical calculations, the bulk lattice was assumed to be infinitely large, but for experiments and finite element simulations, a lattice with 3 x 3 x 3 unit cells was used to represent the bulk lattice. Linear trends have also been included as a reference to highlight the nonlinear nature of the stress-strain curves. (Insets) Magnified sections of the respective figures showing the experimental elastic responses of the lattices. Poisson's ratios of the lattice, ν, vs strain for (c) unit-cell lattice (P-P orientation, e/a = 2/3, L/a = 10/3, w/a = 1/3) and (d) bulk lattice (e/a = 2/3, L/a = 5, w/a = 1/3). No experimental data is available for ν, as the positions of the truss centroids could not be reliably measured due to out-of-plane twisting. Photographic images of the Ti6Al4V unit-cell lattice and 3 x 3 x 3 lattice used in experiments are depicted next to the headings at the top of the figure.

5.2. Size-Dependent Symmetry

Based on the brief qualitative discussion in "Design" section, the 3ATC structure is expected to exhibit asymmetric properties about the *X*, *Y* and *Z* axes when the lattice consists of only a single unit cell, but these properties would be symmetric in an infinitely large lattice. This hypothesis was examined in detail using analytical calculations (black data points), finite

element simulations (hollow data points) and experiments (solid data points), and the results are presented in Fig. 4.

As can be seen, both E and ν do indeed start off asymmetrically for a 1 x 1 x 1 lattice (the unit-cell lattice), with the ***D-D*** orientation showing the highest E/E_s and most positive ν values and ***P-P*** orientation exhibiting the lowest E/E_s and most negative ν values. As the lattice increases in size, these properties converge rapidly and stabilize, becoming orientation- and size- independent when the lattice size is 3 x 3 x 3, which suggests that this is the minimum lattice size that can be approximated as an infinite lattice.

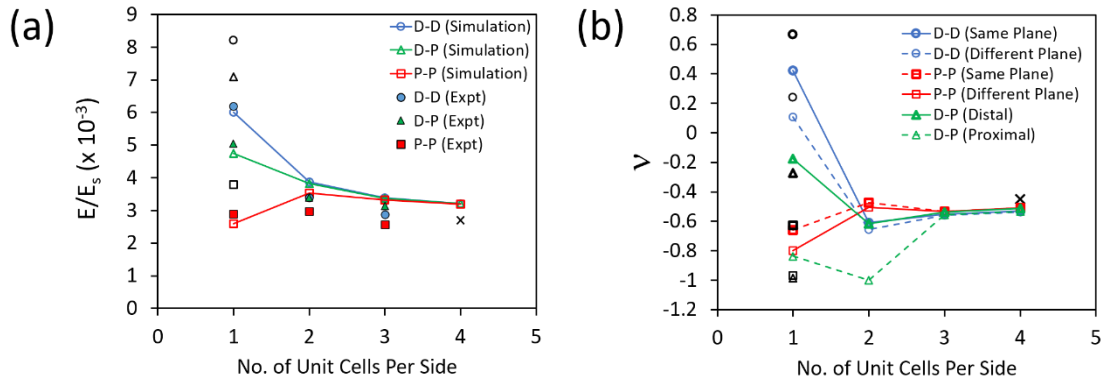

Figure 4: (a) Relative modulus, E/E_s, and (b) lattice Poisson's ratio, ν, for different number of unit cells in an anti-tetrachiral lattice where e/a = 2/3, w/a = 1/3 and L/a = 4/3. If the number of unit cells per side = 3, then the lattice comprises of 3 x 3 x 3 unit cells or 6 x 6 x 6 sub-unit cells. The coloured trends and hollow data points are obtained from finite element simulations. The black hollow data points represent values calculated for the unit-cell lattice using the analytical model. The black cross represents the calculated value for a bulk (infinite) lattice. Experimental data is represented by solid data points.

5.3. Relationship between Elastic Response and Relative Density

5.3.1. Variations in e *and* L

By varying the positional eccentricity, e, and length, L, of the trusses in the unit-cell lattices, it can be observed that the relative modulus, E/E_s, is always the highest for the ***D-D*** orientation, followed by the ***D-P*** orientation and lastly, the ***P-P*** orientation (Fig. 5). The difference between the orientations decreases with decreasing e, which is expected as the

geometrically asymmetric 3ATC unit cell approaches a simple cubic unit cell with cubic symmetry as $e \rightarrow 0$ [4]. Nevertheless, regardless of orientation and eccentricity, E/E_s for the unit-cell lattice is always higher than that for an infinite lattice.

In addition, E/E_s has an approximately linear relationship with relative density, ρ/ρ_s, for all orientations of the unit-cell lattice and the infinite lattice as well. This relationship is similar to that of stretch-dominated designs such as the octet truss structure [50,51], although the coefficients are generally lower for the 3ATC structures.

Similar to E/E_s, the lattice Poisson's ratios, v, are most positive for the ***D-D*** orientation and most negative for the ***P-P*** orientation, and the difference between the orientations decreases with decreasing e (Fig. 6). For the ***D-D*** and ***P-P*** geometries, v is always more positive when the vertical boundary truss (Truss I) and the horizontal truss (Truss II) are in the same plane. For the ***D-P*** geometry, where the horizontal truss is always in a different plane from the vertical boundary truss, v is more positive when the horizontal truss is distal.

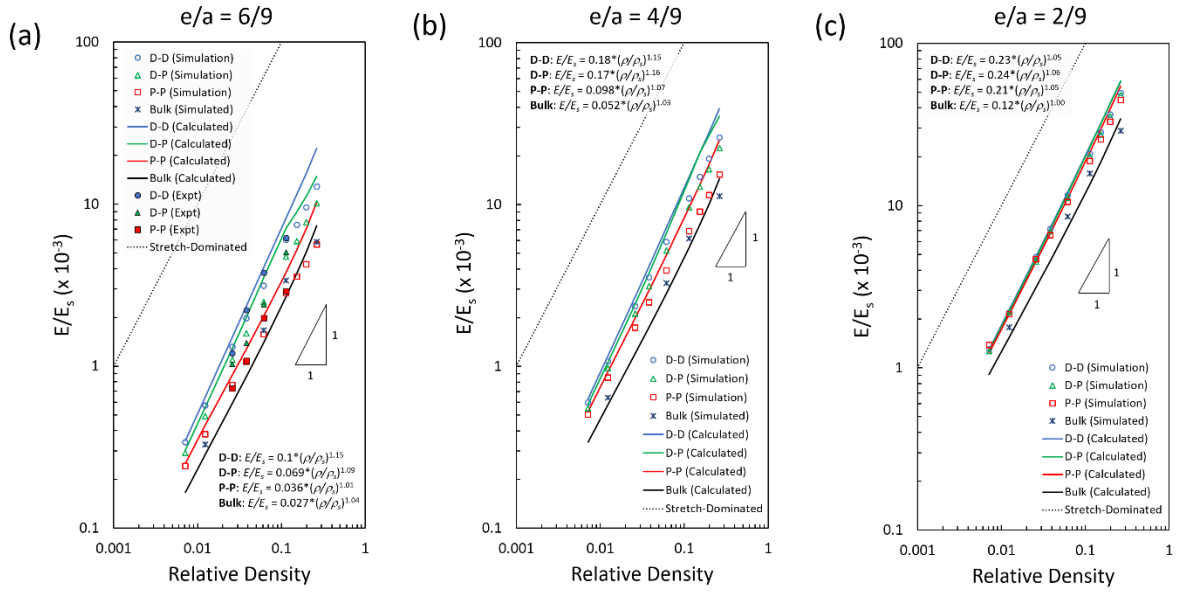

Figure 5: Log-log plots of the relative modulus, E/E_s, vs relative density, ρ/ρ_s, for (a) e/a = 6/9 (b) e/a = 4/9 (c) e/a = 2/9. Variation in relative density for each of the e/a values was achieved by varying L/a independently. The stretch-dominated trend refers to the case where $E/E_s = \rho/\rho_s$.

Compared to the bulk lattice, any orientation involving a distal horizontal truss will generally exhibit a value of v that is more positive. Conversely, if the orientation involves a proximal horizontal truss, then v will likely be more negative than the bulk value. The exact v - ρ/ρ_s relationships, however, are less straightforward, although it can be noted that v increases (*i.e.* becomes more positive) and approaches an asymptotic value with increasing relative density for orientations involving distal horizontal trusses, and vice versa for those involving proximal horizontal trusses (Fig. 6).

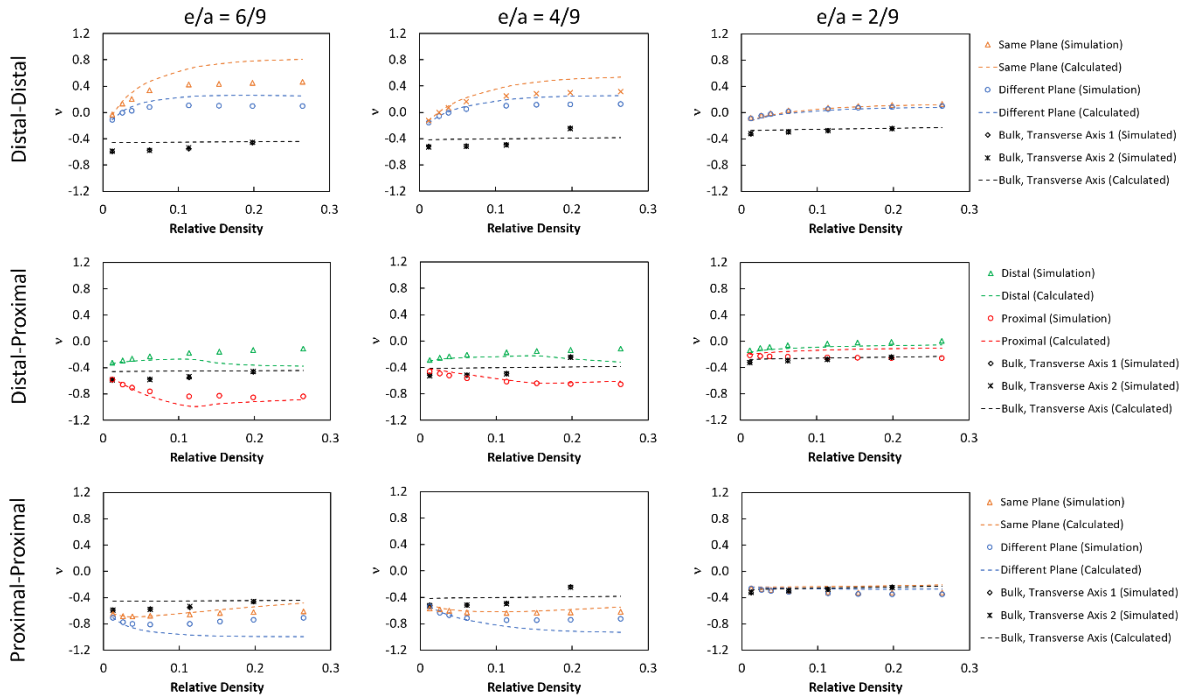

Figure 6: Lattice Poisson's ratio, v, vs relative density, ρ/ρ_s, for different e/a values and orientations of the unit-cell lattice. Relative density in each plot was achieved by varying L/a. The legend for each row is presented to the right of the figures.

5.3.2. Variations in w *and* L

Because the mechanics of the 3ATC structure is essentially dependent on 3 dimensionless parameters, w/a, L/a and e/a, it is necessary to independently vary w/a as well, in addition to variations in e/a and L/a above, in order to obtain a more comprehensive catalogue of the 3ATC design's properties.

The results for E/E_s vs. ρ/ρ_s are presented in Fig. 7 and it shows, once again, that the highest E/E_s values belong to the ***D-D*** orientation, followed by ***D-P***, ***P-P*** and bulk lattice. A striking difference, however, is that the E/E_s - ρ/ρ_s relationship is no longer linear. Indeed, it does not even follow a power law relationship, which is a staple characteristic of cellular structures [50,52]. The primary reason for the broken trend is the existence of the central joint, which contributes to the relative density but does not significantly resist strain. As a result, as the trusses become infinitesimally thin (*i.e.* $w \rightarrow 0$), the lattice modulus approaches 0 even though the relative density is non-zero due to the joint volume.

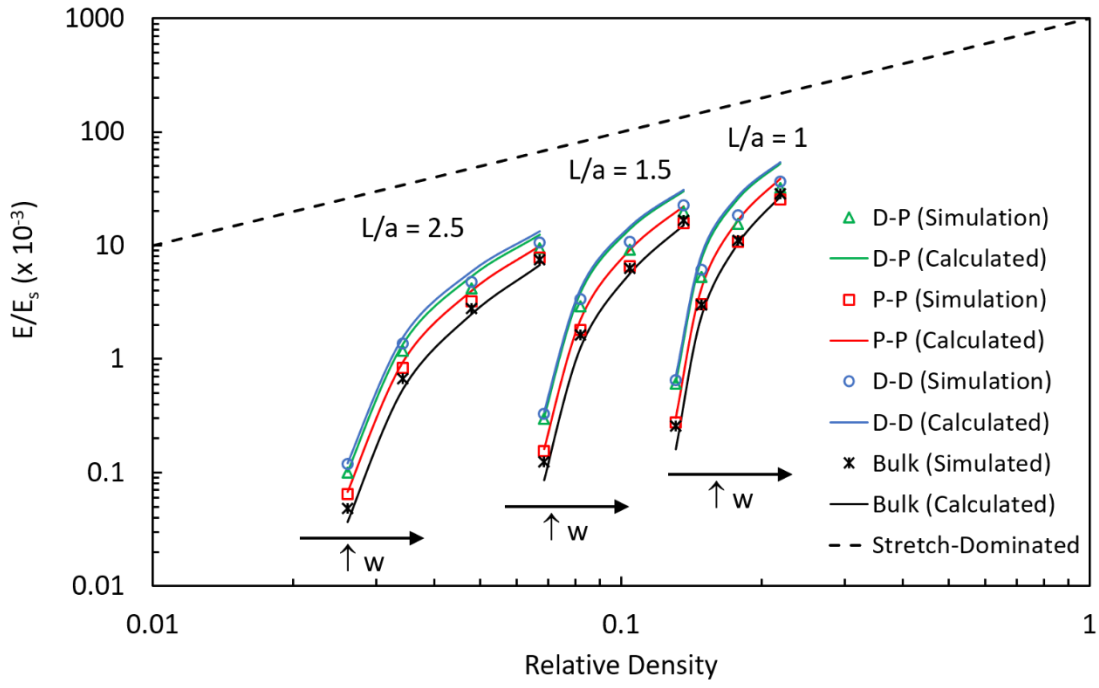

Figure 7: Log-log plots of the relative modulus, E/E_s, vs relative density, ρ/ρ_s, for e/a = 6/9. Variations in relative density for each of the L/a values were achieved by varying w/a independently. The stretch-dominated trend refers to the case where $E/E_s = \rho/\rho_s$.

As for the Poisson's ratios (Fig. 8), the results here are generally consistent with those observed for variations in e and L, although there is one major difference – the v - ρ/ρ_s trends now have v falling towards an asymptotic value with increasing relative density for the ***D-D*** orientation and vice versa for the ***D-P*** and ***P-P*** orientations.

Furthermore, we note that the values of v exhibited by the unit-cell 3ATC lattices here range from -1.2 to 1, which does not fall within the traditional range of -1 to 0.5 [53]. The main reason is that the latter range is only applicable to isotropic solid materials, but as established above, these unit-cell lattices are neither solid nor isotropic. Previous work with auxetic cellular materials and anisotropic materials have demonstrated Poisson's ratios up to -10 [3] and -60 [54] respectively.

It is also worth noting that previous analyses on 3ATC lattices suggested that the Poisson's ratio for a bulk lattice is -1 [5], similar to the case for 2D anti-tetrachiral structures [37]. Based on the "bulk" trends in Fig. 6 and Fig. 8, however, this is clearly not true, because unlike the case for 2D, the strain in the loading direction is an addition of the 2 rotational strains in the 2 transverse planes, whereas the transverse strain in each transverse plane comes from only 1 rotational strain. In other words, from Eq. (94) and (96), $v \approx -0.5$ for a bulk lattice, assuming that the compressive and indentation contributions of Δ_i and Δ_c are small compared to Δ_r.

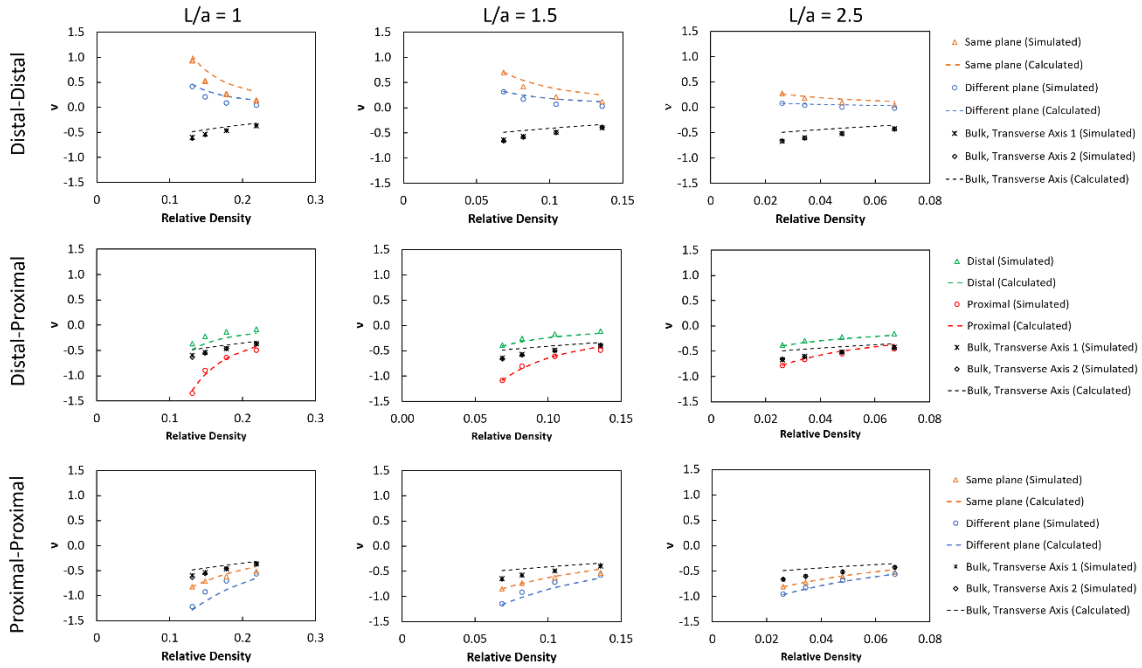

Figure 8: Lattice Poisson's ratio, ν, vs relative density, ρ/ρ_s, for different L/a values and orientations of the unit-cell lattice. Relative density in each plot was achieved by varying w/a. The legend for each row is presented to the right of the figures.

5.4. Rotation-Dominated Deformation

In general, there is very good agreement between the predictions of the analytical model and results from finite element simulations and experiments in Fig. 5 - 10, except when the relative density is large, which implies that the trusses have low aspect ratios (L/w), with deformation behaviors that are not well described by the Euler-Bernoulli equations used in the model. Beyond its efficacy at predicting the elastic response of 3ATC structures, however, the true value of the analytical model is that it provides valuable insights about the structures that would otherwise be difficult to access. One of these insights is the contribution of the various deformation modes, specifically, joint rotation, to the elastic response of the structures. We can define this contribution mathematically as a fraction,

$$f_{rot} = \frac{\varepsilon_r}{\varepsilon} = \frac{\Delta_r}{\Delta_r + \Delta_i + \Delta_c} \tag{102}$$

where ε_r refers to the loading strain caused by joint rotation alone.

From Fig. 9a to Fig. 9c, it can be observed that f_{rot} increases with increasing strain (ε), increasing positional eccentricity (e) and increasing aspect ratio (L/w) of the trusses, as well as decreasing lattice size. The result in Fig. 9a is helpful in understanding the elastic stress-strain response of the 3ATC lattice – as the strain increases, f_{rot} increases and there is a shift from stretch deformation (high E) towards rotation deformation (low E), leading to the asymptotic nonlinear stress-strain trend observed in Fig. 3a.

In addition, if we arbitrarily define a rotation-dominated deformation to be $f_{rot} \geq 0.8$ (*i.e.* joint rotation contributes to 80% of the strain or more), then the majority of the lattices in Fig. 5 with $e/a = 6/9$ are rotation-dominated, those with $e/a = 4/9$ are rotation/stretch co-dominated (*i.e.* $0.2 \leq f_{rot} < 0.8$) and those with $e/a = 2/9$ are stretch-dominated (*i.e.* $f_{rot} < 0.2$) (Fig. 9b). On the other hand, the lattices in Fig. 7, 10 and 11c, where w was varied, are either rotation-dominated or rotation/stretch co-dominated.

Going further and examining Eq. (94), (96) and (102), we note an interesting relationship between f_{rot} and ν for the bulk lattice, which can be summarized as

$$f_{rot} = \frac{\Delta_r}{\Delta_r+\Delta_i+\Delta_c} = \frac{2e|\theta_{T1}|}{\Delta_r+\Delta_c+\Delta_i} = -2\nu \tag{103}$$

Again, if we arbitrarily define a rotation-dominated deformation to be $f_{rot} \geq 0.8$, then any 3ATC structures with $\nu \leq -0.4$ would exhibit a rotation-dominated deformation according to the above equation. This convenient result suggests that the topology of a bulk 3ATC structure can be easily determined, simply by measuring its Poisson's ratio empirically. This may be particularly useful in assessing the topology of disordered auxetic structures with chiral microstructures [3], for which theoretical calculations on f_{rot} may be difficult to perform. Unlike the bulk lattice, however, there is no simple, empirically useful relationship between f_{rot} and ν for the unit-cell lattice.

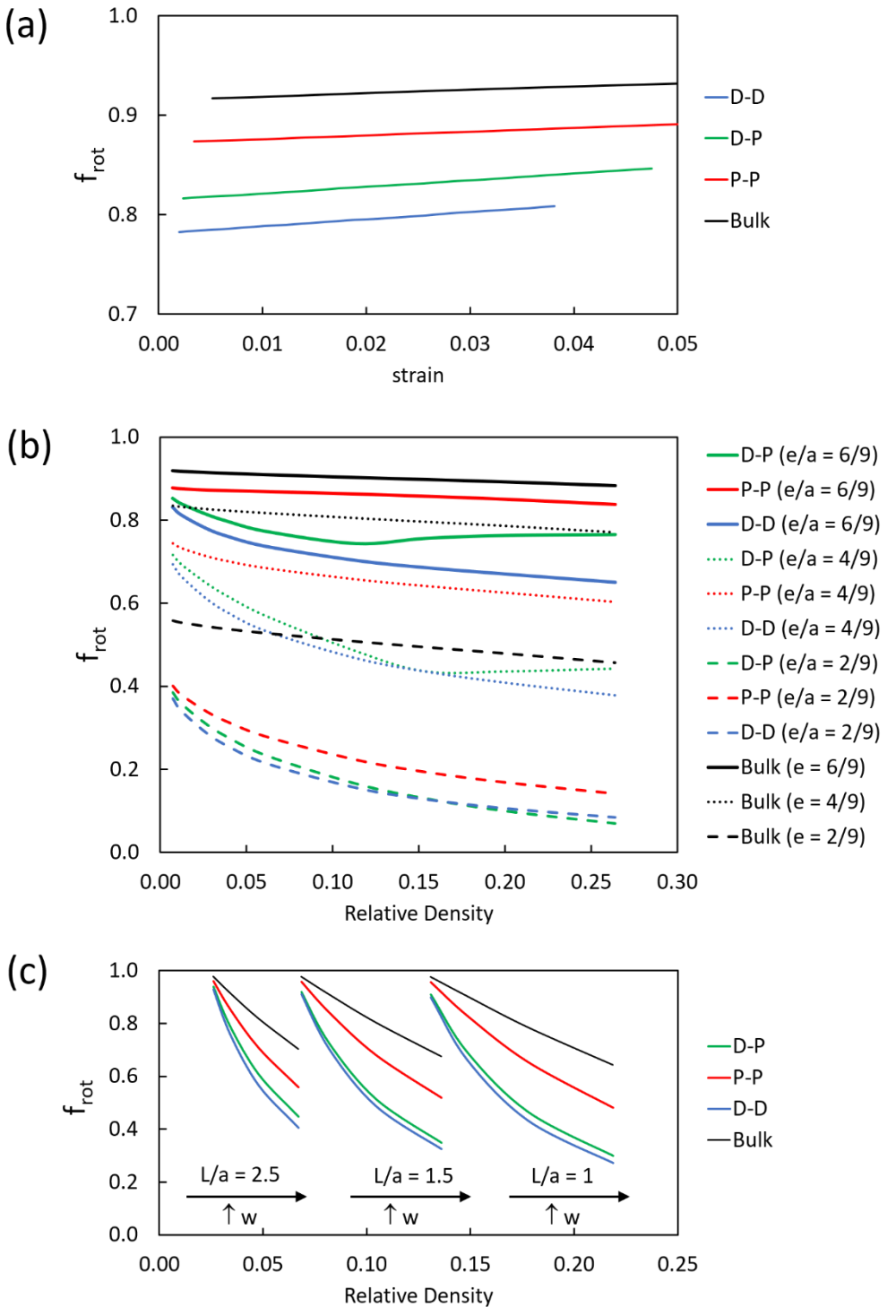

Figure 9: Calculated trends for the fraction of overall lattice strain that is contributed by joint rotation, f_{rot}, vs (a) strain, for the geometry where e/a = 2/3, w/a = 1/3, L/a = 10/3 (b) relative density, ρ/ρ_s, which was varied through L/a for 3 different e/a values and (c) relative density, varied through w/a for 3 different L/a values.

6. Discussion

Based on the results presented, it is clear that, in addition to the well-known bending-dominated and stretch-dominated topologies, there exists a third classification of geometry for cellular materials – the rotation-dominated topology. For such geometries, the main contribution to deformation is through the rotation of a rigid joint, which draws (pushes) the ends of the trusses closer (further), leading to strain.

Using the 3ATC structure as an example, it was found that rotation-dominated or co-dominated structures, regardless of lattice size, can exhibit a unique nonlinear elastic stress-strain response and two distinct E/E_s - ρ/ρ_s relationships – one that is linear, when w/a is fixed, and another that is discontinuous and does not follow simple mathematical expressions, when e/a is fixed. For the linear E/E_s - ρ/ρ_s relationships, the relative stiffness for rotation-dominated structures ($f_{rot} \geq 0.8$) can be lower or equal to that of the stretch-dominated octet-truss geometry ($E/E_s \propto 0.11\rho/\rho_s$) [51] and auxetic re-entrant structures at the same relative density ($E/E_s \sim 0.01 – 0.2$ for $0.1 \leq \rho/\rho_s \leq 0.3$) [10]. On the other hand, the rotation-dominated 3ATC structures tend to exhibit greater auxeticity, particularly for the ***P-P*** orientation ($\nu < -0.4$) and bulk lattice ($\nu \sim -0.5$) (Fig. 6, $e/a = 6/9$), than the re-entrant design for the same relative density ($\nu \sim -0.2$ for $0.1 \leq \rho/\rho_s \leq 0.3$) [10].

Other than the novelty of such properties, these results have important practical significance. For instance, powder compacted materials have previously been found to exhibit E/E_s values that are much lower than those predicted by the bending-dominated and stretch-dominated models, but well in the range of that for 3ATC structures [55–57]. Thus far, these low values have usually been attributed to defects in the supposedly bending-dominated microstructures of the powder compacted materials [55]. However, the work here suggests that the microstructures may actually belong to an entirely different category of geometry – that of

the rotation-dominated topology. Such a microstructure can potentially be further confirmed through measurements of the stress-strain response, which would be nonlinear for a rotation-dominated topology and linear for a stretch- or bending- dominated structure.

Our analysis on f_{rot} also clearly shows that 3ATC structures are not necessarily limited to being rotation-dominated. In fact, a large number of lattices investigated here are rotation-/stretch- co-dominated (e/a = 4/9) and even stretch-dominated (e/a = 2/9). Interestingly, stretch-dominated designs are generally not expected to exhibit negative Poisson's ratio [58], but Fig. 6 (e/a = 2/9) clearly shows that stretch-dominated 3ATC structures can be auxetic as well. For the 3ATC structure, the transition from a rotation-dominated geometry (desirable for its energy absorption efficiency [4]) to a stretch-dominated geometry (desirable for its load-bearing efficiency [50]) can be achieved by reducing the aspect ratio of the trusses, L/w, the positional eccentricity, e, and/ or the lattice size (*i.e.* number of unit cells in the lattice). These geometrical changes reduce the motivation for joint rotation and shifts the deformation mode towards axial loading *i.e.* become more stretch-dominated. This interplay between constraints and deformation mode is essentially the same principle behind Maxwell's stability criterion, which was adapted by Ashby for his analysis of the mechanical behaviour of cellular materials [50].

The effect of reducing the number of unit cells in the lattice to transit towards a stretch-dominated structure can also be understood in this light. With lesser unit cells, the influence of edge constraints (clamped boundary conditions for this study) is much stronger on the deformation of the structure (compare Fig. 1c and 1d). These additional constraints, acting through the shear forces, V_x and V_z, make it harder for the joint to rotate at the same load compared to the bulk lattice, leading to a higher E for the unit-cell lattices. This size-dependent trend for E is in line with results obtained with stretch-twist and bending-dominated geometries [59–62]. Furthermore, our analysis was able to provide a mechanistic understanding of the size effects in 3ATC, demonstrating how they really originate from edge effects, similar to other

lattice designs [63], an insight that is not as readily discernible in previous analyses that employed Cosserat elasticity to empirically characterize micropolar lattices as a whole [64–66].

Similarly, geometries involving distal horizontal trusses, as well as "same-plane" configurations, exhibit higher E values because of stricter constraints. This can be observed from Eq. (44) and Eq. (A7) (refer to Appendix), where it can be seen that the horizontal displacement arising from joint rotation for the distal and proximal trusses are $(a/2 + e/2)\theta_D$ and $(a/2 - e/2)\theta_P$ respectively. This means that for a given horizontal displacement due to joint rotation that can be accommodated by the end deflection of the boundary Truss I *i.e.* $(a/2 + e/2)\theta_D = (a/2 - e/2)\theta_P$, the joint attached to a distal truss will rotate through a smaller angle, θ, than that with a proximal truss *i.e.* $\theta_D < \theta_P$. In the same way, for the "different plane" configurations, part of the horizontal displacement created by the in-plane joint rotation, $e\theta$, can offset by the additional space borne out of the out-of-plane rotation, $e\phi$, and therefore, for the same load that creates the same end deflection of Truss I, the "same plane" joint will rotate through a smaller angle, θ, leading to a smaller strain, than its "different plane" counterpart *i.e.* "same plane" configuration is stiffer than "different plane" configuration.

The presence of the shear forces from the clamped boundaries in a unit cell also led directly to rotation of the joint in all 3 planes under uniaxial loading, which is distinctly different from those in a bulk 3ATC lattice, which only rotate in 2 transverse planes. The additional out-of-plane rotation of the joint, ϕ, enhances the auxetic behaviour in the ***P-P*** and ***D-P*** geometries (*i.e.* ϕ rotation draws the horizontal trusses further in) but counteracts that in the ***D-D*** geometry (*i.e.* ϕ rotation pushes the horizontal trusses outwards). For this reason, ν was found to vary from negative ($|\theta| > |\phi|$) to positive ($|\theta| < |\phi|$) values for ***D-D*** cases while ν for ***P-P*** geometries can become highly negative. The restriction in rotation for joints with distal trusses led directly to a less negative ν for the ***D-P*** (distal) geometries (Fig. 6 and Fig. 8). Similar restrictions for

joint rotation in the "same plane" configuration also led to more positive ν values for such geometries.

Lastly, we note that the unique size-dependent symmetric-to-asymmetric transition of 3ATC structures stems from 4 main characteristics of the design. First, the chirality of the sub-unit cell ensures that it has no plane symmetry *i.e.* one-half (A-side) is not the same as the other half (B-side) (Fig. 10a and 12b). Second, the anti-chiral arrangement means that the side of the sub-unit cell that is not carrying any of the uniaxial load will be the same at all the free edges of the lattice. For instance, if the anti-tetrachiral structure in Fig. 10a is loaded vertically, the free, leftmost and rightmost boundaries of the lattice that are not taking load both belong to side A. In contrast, for the chiral structure in Fig. 10b, the left free boundary belongs to side A, while the right free boundary belongs to side B. These two conditions provide the possibility for 2 types of lattice geometries with a single unit cell design – one where the A-sides are at the lattice free edges (if structure in Fig. 10a is loaded vertically) and the other, where the free edges are occupied by the B-sides instead (if structure in Fig. 10a is loaded horizontally).

Thirdly, to ensure that these 2 different geometries occupy perpendicular axes (*e.g.* A-side free edges along the X-axis, and B-side free edges along the Y-axis), the chiral sub-unit cell must have rotational symmetry (Fig. 10a). This requirement also ensures that there will be the same number of A- and B- sides in the bulk lattice for each axis so that the properties will be symmetric in a large lattice. In other words, the lattice should not be made up of A- and B-sides in one axis, but C- and D- sides in the other axis.

Fourthly, once the sub-unit cells are assembled into the anti-chiral unit cells, these unit cells must not have rotational symmetry beyond an order of 2. In other words, it should not be possible to reproduce the geometry of the anti-chiral unit cell in a particular axis simply by rotating the geometry from another axis. If this is possible, both the unit cell and bulk lattice would have cubic symmetry (Fig. 10b-12d).

In short, for a lattice to exhibit a symmetric-to-asymmetric transition in the X-, Y- and Z- axes as the number of unit cells decreases, its sub-unit cell must have only rotational symmetry (Condition 1) without plane symmetry (Condition 2), be assembled in the anti-chiral design (Condition 3) and the resultant unit cell must have cubic asymmetry (Condition 4).

Interestingly, to the best of our knowledge, the only common design that currently satisfies all of the 4 requirements above is the anti-tetrachiral structure (both 2D and 3D) and therefore, it appears that the symmetric-to-asymmetric transition is unique to this geometry. However, if such a transition is undesirable for any reason, we have shown in our results that the asymmetry at small lattice sizes can be reduced by decreasing the positional eccentricity, *e*, and/ or aspect ratio, *L/w*, of the trusses, in order to minimize the chirality of the design *i.e.* make the A- and B- halves resemble each other more.

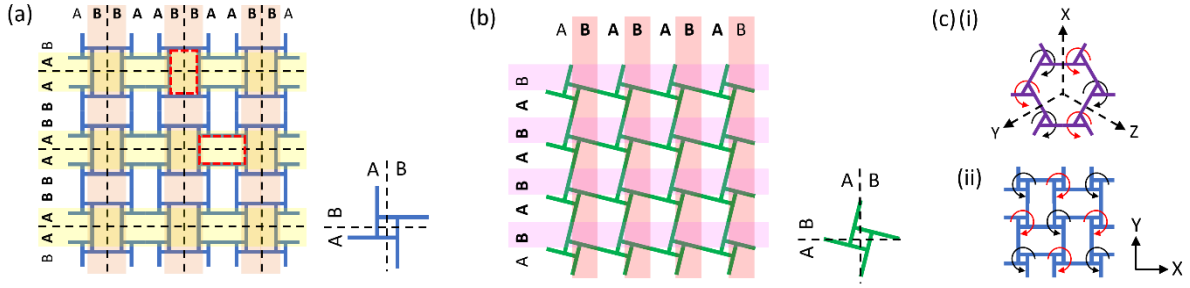

Figure 10: Schematic diagram displaying the arrangement of sub-unit/ unit cells in a (a) anti-tetrachiral and (b) tetrachiral lattice. For the anti-tetrachiral lattice, 6 B-sides and 4 A-sides of the sub-unit cell are bearing load (highlighted in bold) if the lattice is loaded vertically. If it is loaded horizontally, 6 A-sides and 4 B-sides would be bearing load. Therefore, the anti-tetrachiral lattice is anisotropic. For the tetrachiral lattice, the same number of A-sides and B-sides are bearing load regardless of the axis the loading is applied. (c) (i) An anti-trichiral lattice unit cell. (ii) a unit cell that can be tessellated to obtain the same lattice depicted in (a). Note that this unit cell is not anti-chiral, as it has a net anti-clockwise chirality. Both unit cells have rotational symmetry and therefore, they will not exhibit the symmetric-to-asymmetric transition with decreasing lattice size.

7. Conclusions

In this study, we have investigated the elastic modulus and Poisson's ratios of the 3D anti-tetrachiral (3ATC) design with respect to variations in its geometrical parameters and

lattice size, in the limit of infinitesimally small load/ strain, using analytical, numerical and experimental techniques. Our results strongly indicate that the 3ATC design belongs to a third geometrical class, which is distinct from the well-known bending- and stretch- dominated topologies. Designs belonging to this rotation-dominated topology deform primarily through rigid joint rotations, with their defining characteristics being a nonlinear elastic stress-strain curve and a *relative modulus* vs. *relative density* relationship that can be linear or disjointed (does not follow simple mathematical relations). Rotation-dominated structures can also exhibit negative Poisson's ratios which, for the bulk 3ATC design, is approximately -0.5, and equal to half of the contribution of joint rotation to the overall lattice strain. A shift from rotation-domination to stretch-dominance can be accomplished for the 3ATC design by adding constraints to joint rotation, such as reducing the eccentricity of the truss positions, aspect ratio of the trusses and the lattice size.

Furthermore, our analysis has laid down 4 traits that a design should have if it were to exhibit the size-dependent asymmetric-to-symmetric transition – (i) the design should be made up of chiral sub-unit cells, (ii) arranged in an anti-chiral manner, (iii) the chiral sub-unit cells should have rotational symmetry, but (iv) the unit cell they make up should not. Thus far, only the anti-tetrachiral geometry is known to satisfy all these requirements, and the asymmetric-to-symmetric transition with decreasing lattice size was demonstrated for the 3ATC geometry here. In addition, with reduced lattice size, the edge constraints exert a bigger influence on the unit cells in the lattice, making joint rotations more difficult and giving the lattice a correspondingly higher modulus in certain orientations. However, the joint rotation in a unit-cell lattice took place in 3 planes, compared to 2 for the bulk lattice, and the additional out-of-plane rotation was found to add to the auxetic behaviour of the 3ATC structure in certain orientations, and reduce it in others. For this reason, Poisson's ratios for the unit-cell 3ATC structure can range from -1.2 to 1 for the geometric parameters investigated here.

Acknowledgements

Funding for this project was partially provided by C.Q.L.'s Temasek Research Fellowship, for which he gives thanks. Samples for experimental testing were provided by SLM Solutions Singapore Pte Ltd.

References

[1] Prall D, Lakes RS. Properties of a chiral honeycomb with a poisson's ratio of — 1. International Journal of Mechanical Sciences 1997;39:305–14. https://doi.org/10.1016/S0020-7403(96)00025-2.

[2] Wu W, Hu W, Qian G, Liao H, Xu X, Berto F. Mechanical design and multifunctional applications of chiral mechanical metamaterials: A review. Materials & Design 2019;180:107950. https://doi.org/10.1016/j.matdes.2019.107950.

[3] Alderson KL, Alderson A, Evans KE. The interpretation of the strain-dependent Poisson's ratio in auxetic polyethylene: The Journal of Strain Analysis for Engineering Design 2005. https://doi.org/10.1243/0309324971513346.

[4] Lai CQ, Daraio C. Highly Porous Microlattices as Ultrathin and Efficient Impact Absorbers. International Journal of Impact Engineering 2018;120:138–49.

[5] Xia R, Song X, Sun L, Wu W, Li C, Cheng T, et al. Mechanical Properties of 3D Isotropic Anti-Tetrachiral Metastructure. Physica Status Solidi (b) 2018;255:1700343. https://doi.org/10.1002/pssb.201700343.

[6] Hassan MR, Scarpa F, Ruzzene M, Mohammed NA. Smart shape memory alloy chiral honeycomb. Materials Science and Engineering: A 2008;481–482:654–7. https://doi.org/10.1016/j.msea.2006.10.219.

[7] Budarapu PR, Y B SS, Natarajan R. Design concepts of an aircraft wing: composite and morphing airfoil with auxetic structures. Front Struct Civ Eng 2016;10:394–408. https://doi.org/10.1007/s11709-016-0352-z.

[8] Grima JN, Caruana-Gauci R, Attard D, Gatt R. Three-dimensional cellular structures with negative Poisson's ratio and negative compressibility properties. Proceedings of the Royal Society A: Mathematical, Physical and Engineering Sciences 2012;468:3121–38. https://doi.org/10.1098/rspa.2011.0667.

[9] Mir M, Ali MN, Sami J, Ansari U. Review of Mechanics and Applications of Auxetic Structures. Advances in Materials Science and Engineering 2014;2014:e753496. https://doi.org/10.1155/2014/753496.

[10] Yang L, Harrysson O, West H, Cormier D. Mechanical properties of 3D re-entrant honeycomb auxetic structures realized via additive manufacturing. International Journal of Solids and Structures 2015;69–70:475–90. https://doi.org/10.1016/j.ijsolstr.2015.05.005.

[11] Lu Q, Qi D, Li Y, Xiao D, Wu W. Impact energy absorption performances of ordinary and hierarchical chiral structures. Thin-Walled Structures 2019;140:495–505. https://doi.org/10.1016/j.tws.2019.04.008.

[12] Wang Q, Yang Z, Lu Z, Li X. Mechanical responses of 3D cross-chiral auxetic materials under uniaxial compression. Materials & Design 2020;186:108226. https://doi.org/10.1016/j.matdes.2019.108226.

[13] Alderson KL, Webber RS, Mohammed UF, Murphy E. An experimental study of ultrasonic attenuation in microporous polyethylene. Applied Acoustics 1997;50:23–33. https://doi.org/10.1016/S0003-682X(96)00023-0.

[14] Bacigalupo A, Gnecco G, Lepidi M, Gambarotta L. Optimal design of low-frequency band gaps in anti-tetrachiral lattice meta-materials. Composites Part B: Engineering 2017;115:341–59. https://doi.org/10.1016/j.compositesb.2016.09.062.

[15] Vadalà F, Bacigalupo A, Lepidi M, Gambarotta L. Bloch wave filtering in tetrachiral materials via mechanical tuning. Composite Structures 2018;201:340–51. https://doi.org/10.1016/j.compstruct.2018.05.117.

[16] Wu L, Li B, Zhou J. Isotropic Negative Thermal Expansion Metamaterials. ACS Appl Mater Interfaces 2016;8:17721–7. https://doi.org/10.1021/acsami.6b05717.

[17] Li H, Ma Y, Wen W, Wu W, Lei H, Fang D. In Plane Mechanical Properties of Tetrachiral and Antitetrachiral Hybrid Metastructures. J Appl Mech 2017;84. https://doi.org/10.1115/1.4036937.
[18] Steffens F, Oliveira FR, Mota C, Fangueiro R. High-performance composite with negative Poisson's ratio. Journal of Materials Research 2017;32:3477–84. https://doi.org/10.1557/jmr.2017.340.
[19] Spadoni A, Ruzzene M. Numerical and experimental analysis of the static compliance of chiral truss-core airfoils. Journal of Mechanics of Materials and Structures 2007;2:965–81. https://doi.org/10.2140/jomms.2007.2.965.
[20] Airoldi A, Bettini P, Panichelli P, Oktem MF, Sala G. Chiral topologies for composite morphing structures – Part I: Development of a chiral rib for deformable airfoils. Physica Status Solidi (b) 2015;252:1435–45. https://doi.org/10.1002/pssb.201451689.
[21] Airoldi A, Bettini P, Panichelli P, Sala G. Chiral topologies for composite morphing structures – Part II: Novel configurations and technological processes. Physica Status Solidi (b) 2015;252:1446–54. https://doi.org/10.1002/pssb.201584263.
[22] Bettini P, Airoldi A, Sala G, Landro LD, Ruzzene M, Spadoni A. Composite chiral structures for morphing airfoils: Numerical analyses and development of a manufacturing process. Composites Part B: Engineering 2010;41:133–47. https://doi.org/10.1016/j.compositesb.2009.10.005.
[23] Farrugia P-S, Gatt R, Grima JN. A Novel Three-Dimensional Anti-Tetrachiral Honeycomb. Physica Status Solidi (b) 2019;256. https://doi.org/10.1002/pssb.201800473.
[24] Günaydın K, Eren Z, Kazancı Z, Scarpa F, Grande AM, Türkmen HS. In-plane compression behavior of anti-tetrachiral and re-entrant lattices. Smart Mater Struct 2019;28:115028. https://doi.org/10.1088/1361-665X/ab47c9.
[25] Wu W, Qi D, Liao H, Qian G, Geng L, Niu Y, et al. Deformation mechanism of innovative 3D chiral metamaterials. Scientific Reports 2018;8:1–10. https://doi.org/10.1038/s41598-018-30737-7.
[26] Jonathan R, Kazuto T, Fabrizio S, Peter W, Toshiharu M. Shape memory polymer hexachiral auxetic structures with tunable stiffness. Smart Materials and Structures 2014;23:1–11.
[27] Hu LL, Wu ZJ, Fu MH. Mechanical behavior of anti-trichiral honeycombs under lateral crushing. International Journal of Mechanical Sciences 2018;140:537–46. https://doi.org/10.1016/j.ijmecsci.2018.03.039.
[28] Hu LL, Luo ZR, Zhang ZY, Lian MK, Huang LS. Mechanical property of re-entrant anti-trichiral honeycombs under large deformation. Composites Part B: Engineering 2019;163:107–20. https://doi.org/10.1016/j.compositesb.2018.11.010.
[29] Sha ZD, She CM, Xu GK, Pei QX, Liu ZS, Wang TJ, et al. Metallic glass-based chiral nanolattice: Light weight, auxeticity, and superior mechanical properties. Materials Today 2017;20:569–76. https://doi.org/10.1016/j.mattod.2017.10.001.
[30] Jiang Y, Li Y. Novel 3D-Printed Hybrid Auxetic Mechanical Metamaterial with Chirality-Induced Sequential Cell Opening Mechanisms. Advanced Engineering Materials 2018;20:1700744. https://doi.org/10.1002/adem.201700744.
[31] Zhong R, Fu M, Yin Q, Xu O, Hu L. Special characteristics of tetrachiral honeycombs under large deformation. International Journal of Solids and Structures 2019;169:166–76. https://doi.org/10.1016/j.ijsolstr.2019.04.020.
[32] Haghpanah B, Papadopoulos J, Mousanezhad D, Nayeb-Hashemi H, Vaziri A. Buckling of regular, chiral and hierarchical honeycombs under a general macroscopic stress state. Proceedings of the Royal Society A: Mathematical, Physical and Engineering Sciences 2014;470:20130856. https://doi.org/10.1098/rspa.2013.0856.
[33] Mousanezhad D, Haghpanah B, Ghosh R, Hamouda AM, Nayeb-Hashemi H, Vaziri A. Elastic properties of chiral, anti-chiral, and hierarchical honeycombs: A simple energy-based approach. Theoretical and Applied Mechanics Letters 2016;6:81–96. https://doi.org/10.1016/j.taml.2016.02.004.

[34] Lorato A, Innocenti P, Scarpa F, Alderson A, Alderson KL, Zied KM, et al. The transverse elastic properties of chiral honeycombs. Composites Science and Technology 2010;70:1057–63. https://doi.org/10.1016/j.compscitech.2009.07.008.
[35] Runkel F, Ramstein G, Molinari G, Arrieta AF, Ermanni P. Mechanics of curved-ligament hexachiral metastructures under planar deformations. Journal of the Mechanics and Physics of Solids 2019;125:145–63. https://doi.org/10.1016/j.jmps.2018.12.001.
[36] Chen Y, Liu XN, Hu GK, Sun QP, Zheng QS. Micropolar continuum modelling of bi-dimensional tetrachiral lattices. Proceedings of the Royal Society A: Mathematical, Physical and Engineering Sciences 2014;470:20130734. https://doi.org/10.1098/rspa.2013.0734.
[37] Alderson A, Alderson KL, Attard D, Evans KE, Gatt R, Grima JN, et al. Elastic constants of 3-, 4- and 6-connected chiral and anti-chiral honeycombs subject to uniaxial in-plane loading. Composites Science and Technology 2010;70:1042–8. https://doi.org/10.1016/j.compscitech.2009.07.009.
[38] Clausen A, Wang F, Jensen JS, Sigmund O, Lewis JA. Topology Optimized Architectures with Programmable Poisson's Ratio over Large Deformations. Advanced Materials 2015;27:5523–7. https://doi.org/10.1002/adma.201502485.
[39] Jiang Y, Li Y. 3D Printed Auxetic Mechanical Metamaterial with Chiral Cells and Re-entrant Cores. Scientific Reports 2018;8:1–11. https://doi.org/10.1038/s41598-018-20795-2.
[40] Khare E, Temple S, Tomov I, Zhang F, Smoukov SK. Low Fatigue Dynamic Auxetic Lattices With 3D Printable, Multistable, and Tuneable Unit Cells. Front Mater 2018;5. https://doi.org/10.3389/fmats.2018.00045.
[41] Fu M-H, Zheng B-B, Li W-H. A novel chiral three-dimensional material with negative Poisson's ratio and the equivalent elastic parameters. Composite Structures 2017;176:442–8. https://doi.org/10.1016/j.compstruct.2017.05.027.
[42] Pajunen K, Johanns P, Pal RK, Rimoli JJ, Daraio C. Design and impact response of 3D-printable tensegrity-inspired structures. Materials & Design 2019;182:107966. https://doi.org/10.1016/j.matdes.2019.107966.
[43] Huang H-H, Wong B-L, Chou Y-C. Design and properties of 3D-printed chiral auxetic metamaterials by reconfigurable connections. Physica Status Solidi (b) 2016;253:1557–64. https://doi.org/10.1002/pssb.201600027.
[44] Shen J, Zhou S, Huang X, Xie YM. Simple cubic three-dimensional auxetic metamaterials. Physica Status Solidi (b) 2014;251:1515–22. https://doi.org/10.1002/pssb.201451304.
[45] Ren X, Shen J, Tran P, Ngo TD, Xie YM. Design and characterisation of a tuneable 3D buckling-induced auxetic metamaterial. Materials & Design 2018;139:336–42. https://doi.org/10.1016/j.matdes.2017.11.025.
[46] Ren X, Shen J, Ghaedizadeh A, Tian H, Xie YM. Experiments and parametric studies on 3D metallic auxetic metamaterials with tuneable mechanical properties. Smart Mater Struct 2015;24:095016. https://doi.org/10.1088/0964-1726/24/9/095016.
[47] Elsayed M, Ghazy M, Youssef Y, Essa K. Optimization of SLM process parameters for Ti6Al4V medical implants. Rapid Prototyping Journal 2019;25:433–47. https://doi.org/10.1108/RPJ-05-2018-0112.
[48] Mierzejewska ŻA, Hudák R, Sidun J. Mechanical Properties and Microstructure of DMLS Ti6Al4V Alloy Dedicated to Biomedical Applications. Materials (Basel) 2019;12. https://doi.org/10.3390/ma12010176.
[49] Cheng L, Xia X, Yu W, Scriven LE, Gerberich WW. Flat-punch indentation of viscoelastic material. Journal of Polymer Science Part B: Polymer Physics 2000. https://doi.org/10.1002/(SICI)1099-0488(20000101)38:1<10::AID-POLB2>3.0.CO;2-6.
[50] Ashby MF. The properties of foams and lattices. Philosophical Transactions of the Royal Society of London A: Mathematical, Physical and Engineering Sciences 2006;364:15–30. https://doi.org/10.1098/rsta.2005.1678.

[51] Deshpande VS, Fleck NA, Ashby MF. Effective properties of the octet-truss lattice material. Journal of the Mechanics and Physics of Solids 2001;49:1747–69. https://doi.org/10.1016/S0022-5096(01)00010-2.
[52] Gibson LJ, Ashby MF. Cellular Solids: Structure and Properties. 2 edition. Cambridge: Cambridge University Press; 1999.
[53] Li D, Dong L, Lakes RS. A unit cell structure with tunable Poisson's ratio from positive to negative. Materials Letters 2016;164:456–9. https://doi.org/10.1016/j.matlet.2015.11.037.
[54] Peel LD. Exploration of high and negative Poisson's ratio elastomer-matrix laminates. Physica Status Solidi (b) 2007;244:988–1003. https://doi.org/10.1002/pssb.200572717.
[55] Goodall R. 10 - Porous metals: foams and sponges. In: Chang I, Zhao Y, editors. Advances in Powder Metallurgy, Woodhead Publishing; 2013, p. 273–307. https://doi.org/10.1533/9780857098900.2.273.
[56] Hakamada M, Asao Y, Kuromura T, Chen Y, Kusuda H, Mabuchi M. Density dependence of the compressive properties of porous copper over a wide density range. Acta Materialia 2007;55:2291–9. https://doi.org/10.1016/j.actamat.2006.11.024.
[57] Wen CE, Mabuchi M, Yamada Y, Shimojima K, Chino Y, Asahina T. Processing of biocompatible porous Ti and Mg. Scripta Materialia 2001;45:1147–53. https://doi.org/10.1016/S1359-6462(01)01132-0.
[58] Mitschke H, Schury F, Mecke K, Wein F, Stingl M, Schröder-Turk GE. Geometry: The leading parameter for the Poisson's ratio of bending-dominated cellular solids. International Journal of Solids and Structures 2016;100–101:1–10. https://doi.org/10.1016/j.ijsolstr.2016.06.027.
[59] Andrews EW, Gioux G, Onck P, Gibson LJ. Size effects in ductile cellular solids. Part II: experimental results. International Journal of Mechanical Sciences 2001;43:701–13. https://doi.org/10.1016/S0020-7403(00)00043-6.
[60] Ha CS, Plesha ME, Lakes RS. Chiral three-dimensional lattices with tunable Poisson's ratio. Smart Mater Struct 2016;25:054005. https://doi.org/10.1088/0964-1726/25/5/054005.
[61] Onck PR, Andrews EW, Gibson LJ. Size effects in ductile cellular solids. Part I: modeling. International Journal of Mechanical Sciences 2001;43:681–99. https://doi.org/10.1016/S0020-7403(00)00042-4.
[62] Yang L. A study about size effects of 3D periodic cellular structures. Proceedings of the 27th Annual International Solid Freeform Fabrication Symposium, Austin, Texas: 2016, p. 2181–93.
[63] Yoder M, Thompson L, Summers J. Size effects in lattice structures and a comparison to micropolar elasticity. International Journal of Solids and Structures 2018;143:245–61. https://doi.org/10.1016/j.ijsolstr.2018.03.013.
[64] Reasa DR, Lakes RS. Cosserat Effects in Achiral and Chiral Cubic Lattices. J Appl Mech 2019;86. https://doi.org/10.1115/1.4044047.
[65] Rueger Z, Lakes RS. Strong Cosserat Elasticity in a Transversely Isotropic Polymer Lattice. Phys Rev Lett 2018;120:065501. https://doi.org/10.1103/PhysRevLett.120.065501.
[66] Rueger Z, Li D, Lakes RS. Observation of Cosserat Elastic Effects in a Tetragonal Negative Poisson's Ratio Lattice. Physica Status Solidi (b) 2017;254:1600840. https://doi.org/10.1002/pssb.201600840.

Appendix

A1. Proximal-Proximal (*P-P*) Arrangement

A1.1. *Truss I, II & III*

Comparing Fig. 2a and Fig. A1a, it can be observed that the free body diagrams for Truss I and Truss III are the same in both the ***D-D*** and ***P-P*** geometries. The only difference is that the $+X$ direction is reversed. This was done to keep the *Y-Z* coordinates in Fig. 2 and Fig. A1 constant. Therefore, from Eq. (12) and (13), the deflection and slope of Truss I for the ***P-P*** arrangement are

$$v_I\left[\frac{L}{2}\right] = -\frac{M_I}{F}\left\{1 - \frac{1}{cos\left(\frac{kL}{2}\right)}\right\} - \frac{V_x}{kF}\left\{tan\left(\frac{kL}{2}\right) - \frac{kL}{2}\right\} \tag{A1}$$

$$v_I'\left[\frac{L}{2}\right] = \frac{M_I k}{F} tan\left(\frac{kL}{2}\right) - \frac{V_x}{F}\left\{\frac{1}{cos\left(\frac{kL}{2}\right)} - 1\right\} \tag{A2}$$

while the slope at the end of Truss III, from Eq. (37), is

$$v_{III}'[0] = \frac{M_{III} k}{F} tan\left(\frac{kL}{2}\right) \tag{A3}$$

Note that the signs for the deflection and slopes in Eq. (A1) - (A3) are opposite to that in Eq. (12), (13) and (37) due to the reversal of the *X*-axis orientation. Therefore, $v_I[0]$ is now negative, while $v_I'[0]$ is now positive.

For Truss II (Fig. A1a) and Truss IV (Fig. A1b), we note that V_x and V_z are applied compressively in the ***P-P*** case, rather than in tension in the ***D-D*** arrangement. The free body diagrams for Truss II and Truss IV are therefore, the same as that of Truss III. From Eq. (37), the slope at the end of Truss II can then be obtained as

$$v_{II}'[0] = -\frac{M_{II}\alpha}{\tau_x} tan\left(\frac{\alpha L}{2}\right) \tag{A4}$$

For small V_x (*i.e.* small α), using small angle approximation, Eq. (A4) can be reduced to

$$v_{II}'[0] \approx \frac{M_{II} L}{2E_s I} \tag{A5}$$

which is the same as the ***D-D*** case. In other words, when the axial force acting on a buckled beam is small, the gradient at the end of the truss is dependent only on the magnitude of the concentrated moment.

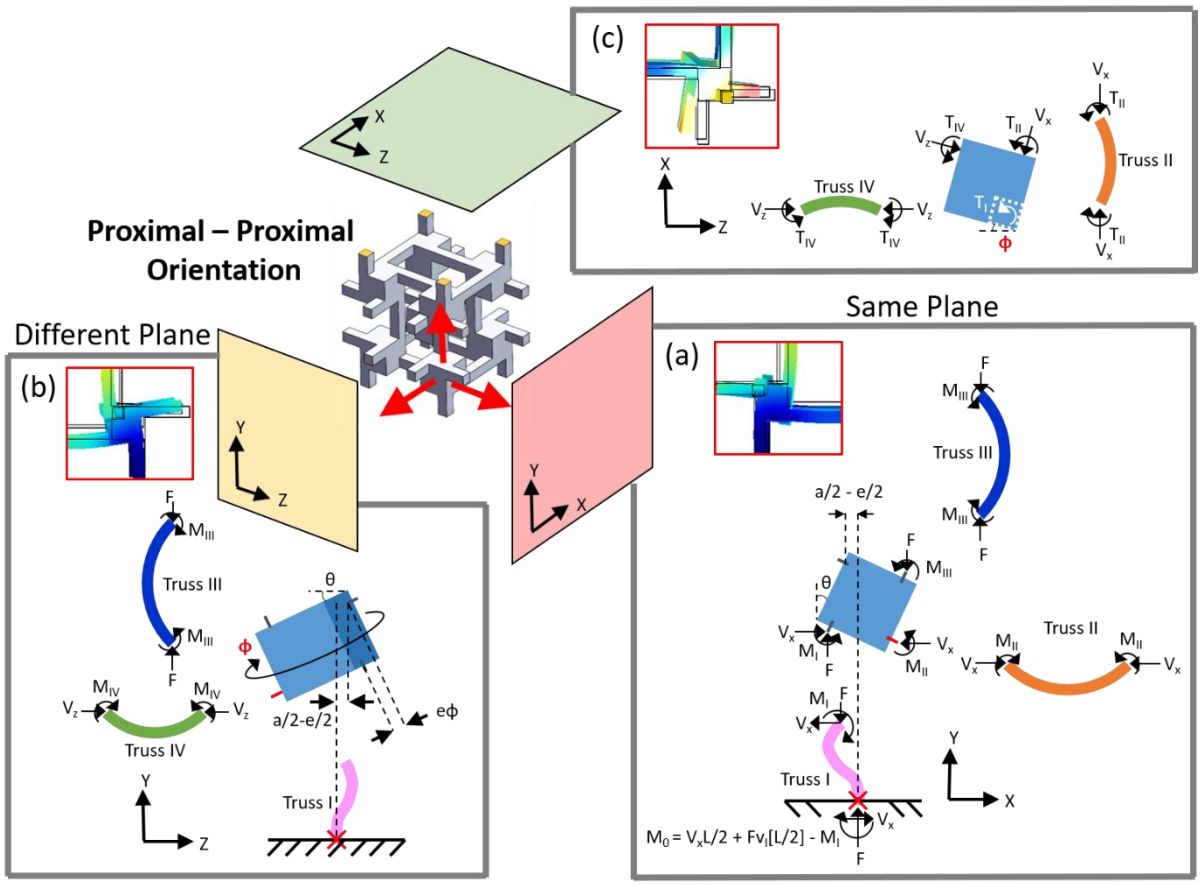

Figure A11: Free-body diagrams of the anti-tetrachiral unit-cell lattice, oriented in such a way that both load-bearing lateral trusses are proximal to the clamped boundaries. The clamped boundaries are highlighted in yellow. The clamping is symmetrical, so the ends of the bottom-most vertical trusses are clamped as well. There are no constraints on the lateral sides of the lattice. The uniaxial load is applied vertically on the clamped surfaces. Because of symmetry, only the free-body diagrams for the bottom sub-unit cell (centre of the 3 red arrows) in different planes are shown. For simplicity, only load-bearing trusses are depicted. The point of origin for Truss I is marked by a red cross. The dashes at the perimeter of the central cubic joint indicate the positions where the trusses join with the cube. The red dash indicates the pivot of rotation i.e. the horizontal position of this point, at the end of the load-bearing lateral truss, is fixed. (a) Transverse Plane 1: The boundary truss, Truss I, is in the same plane as the load-bearing lateral truss, Truss II. (b) Transverse Plane 2: Truss I and the load-bearing lateral truss, Truss IV, are in parallel planes offset by a distance of *e*. (c) Loading Plane: Top view showing the joint and the 2 lateral trusses, II and IV. θ is the in-plane rotation and may be different in (a) and (b). ϕ is the out-of-plane rotation that is the same in all planes (not shown in (a) as it does not impose additional horizontal constraints that will influence θ). (Insets) Images from finite element simulations illustrating the deformation of the sub-unit cell in the respective planes.

A1.2. Equilibrium of Moments about the Rigid Joint

We also note that another difference between the ***D-D*** and ***P-P*** geometries is that the vertical distance between the ends of Truss I and Truss II is *a*/2 + *e*/2 in the ***D-D*** case, compared to *a*/2 - *e*/2 in the ***P-P*** case. Therefore, when considering the equilibrium of moments about the central cube, the solution in Eq. (41) is applicable, as long as *a*/2 + *e*/2 is substituted with *a*/2 - *e*/2, giving

$$M_I + M_{II} + M_{III} + \left(\frac{a}{2} - \frac{e}{2}\right) V_x = Fe \tag{A6}$$

A1.3. Same Plane

When Truss I and II are in the same plane (Fig. A1a), and again, noting that the horizontal coordinate of the end of Truss II is fixed due to conservation of the Truss II's length, from Eq. (42), we make the appropriate substitution of *a*/2 + *e*/2 with *a*/2 - *e*/2 to give the additional constraint,

$$\left(\frac{a}{2} - \frac{e}{2}\right)\left(v_I'\left[\frac{L}{2}\right]\right) + v_I\left[\frac{L}{2}\right] = 0 \tag{A7}$$

Note that $v_I[0]$ is negative, while $v_I'[0]$ is positive here.

Following the procedure for the ***D-D*** geometry, the end gradients of Truss I - III can be equated to express M_{II} and M_{III} in terms of M_I and V_x. Using these equations, together with the constraints in Eq. (A6) and Eq. (A7), we can obtain

$$V_x = \frac{Q_P}{R_P} M_I \tag{A8}$$

$$M_I = \frac{Fe}{2 + S + \frac{Q_P}{R_P}\left(\frac{a}{2} - \frac{e}{2} + U + N\right)} \tag{A9}$$

where Q_D and R_D are modified into Q_P and R_P by substituting *a*/2 + *e*/2 with *a*/2 - *e*/2, that is,

$$Q_P = \left(\frac{a}{2} - \frac{e}{2}\right) k tan\left(\frac{kL}{2}\right) + \frac{1}{cos\left(\frac{kL}{2}\right)} - 1 \tag{A10}$$

$$R_P = \left(\frac{a}{2} - \frac{e}{2}\right)\left(\frac{1}{cos\left(\frac{kL}{2}\right)} - 1\right) + \frac{1}{k}\left(tan\left(\frac{kL}{2}\right) - \frac{kL}{2}\right) \quad \text{(A11)}$$

A1.4. Different Plane

For the case where the fixed and lateral trusses are offset by a distance of *e*, the constraint equation would be

$$\left(\frac{a}{2} - \frac{e}{2}\right)\left(v_I'\left[\frac{L}{2}\right]\right) + v_I\left[\frac{L}{2}\right] - e|\phi| = 0 \quad \text{(A12)}$$

Once again, $a/2 + e/2$ in Eq. (59) is substituted with $a/2 - e/2$ and the sign of $e\phi$ is reversed, following the sign reversal for $v_I[0]$ and $v_I'[0]$ detailed above. The magnitude of ϕ is the same as in the ***D-D*** case and is given by Eq. (58).

Following the strategy outlined in the "same plane" case, Eq. (A1) – (A6) can be solved, together with Eq. (A12), to give

$$V_z = \frac{Q_P}{R_P + \frac{e^2k^2L}{2}\left(\frac{1+\upsilon_S}{3+2\upsilon_S}\right)} M_I \quad \text{(A13)}$$

$$M_I = \frac{Fe}{2 + S + \frac{Q_P}{R_P + \frac{e^2k^2L}{2}\left(\frac{1+\upsilon_S}{3+2\upsilon_S}\right)}\left(\frac{a}{2} - \frac{e}{2} + U + N\right)} \quad \text{(A14)}$$

A1.5. Stress-Strain Relationship

Similar to the ***D-D*** case, Eq. (A7) – (A10), (A13) and (A14) can then be used to obtain the cube rotations, via $v_I'[L/2]$ in Eq. (13) or (A2), to give

$$\theta_{sp} = -\frac{e}{2 + S + \frac{Q_P}{R_P}\left(\frac{a}{2} - \frac{e}{2} + U + N\right)}\left\{-ktan\left(\frac{kL}{2}\right) + \frac{Q_P}{R_P}\left\{\frac{1}{cos\left(\frac{kL}{2}\right)} - 1\right\}\right\} \quad \text{(A15)*}$$

$$\theta_{dp} = \frac{e}{2 + S + \frac{Q_P}{R_P + \frac{e^2k^2L}{2}\left(\frac{1+\upsilon_S}{3+2\upsilon_S}\right)}\left(\frac{a}{2} - \frac{e}{2} + U + N\right)}\left\{-ktan\left(\frac{kL}{2}\right) + \frac{Q_P}{R_P + \frac{e^2k^2L}{2}\left(\frac{1+\upsilon_S}{3+2\upsilon_S}\right)}\left\{\frac{1}{cos\left(\frac{kL}{2}\right)} - 1\right\}\right\} \quad \text{(A16)*}$$

These rotations can then be used to establish the quantitative stress-strain relationship for the ***P-P*** case using Eq. (64) – (67).

A2. Distal-Proximal (*D-P*) Arrangement

A2.1. Rotation in the Loading Plane

When the sub-unit cell is oriented such that there is 1 distal and 1 proximal lateral truss, the free body diagrams for the trusses and cube are essentially the same as the ***D-D*** case. In the ***D-P*** geometry, however, the plane of the fixed boundary truss is always separated from that of the lateral truss by a distance of e and therefore, ϕ is necessary for the analysis of both transverse planes, *X-Y* and *Y-Z*.

In the *X-Z* plane (Fig. A2a), the equilibrium of moments dictates that the torque acting on Truss I be

$$T_I = e(V_P - V_D) - T_D - T_P \tag{A17}$$

where the subscript *D* refers to the distal lateral truss and *P* refers to the proximal lateral truss. Based on the analysis presented in Eq. (52) – (56), we find

$$T_D = T_P = \frac{1+\nu_s}{3+2\nu_s} e(V_P - V_D) \tag{A18}$$

$$\phi = \frac{eL}{2E_s I}\left(\frac{1+\upsilon_s}{3+2\upsilon_s}\right)(V_P - V_D) \tag{A19}$$

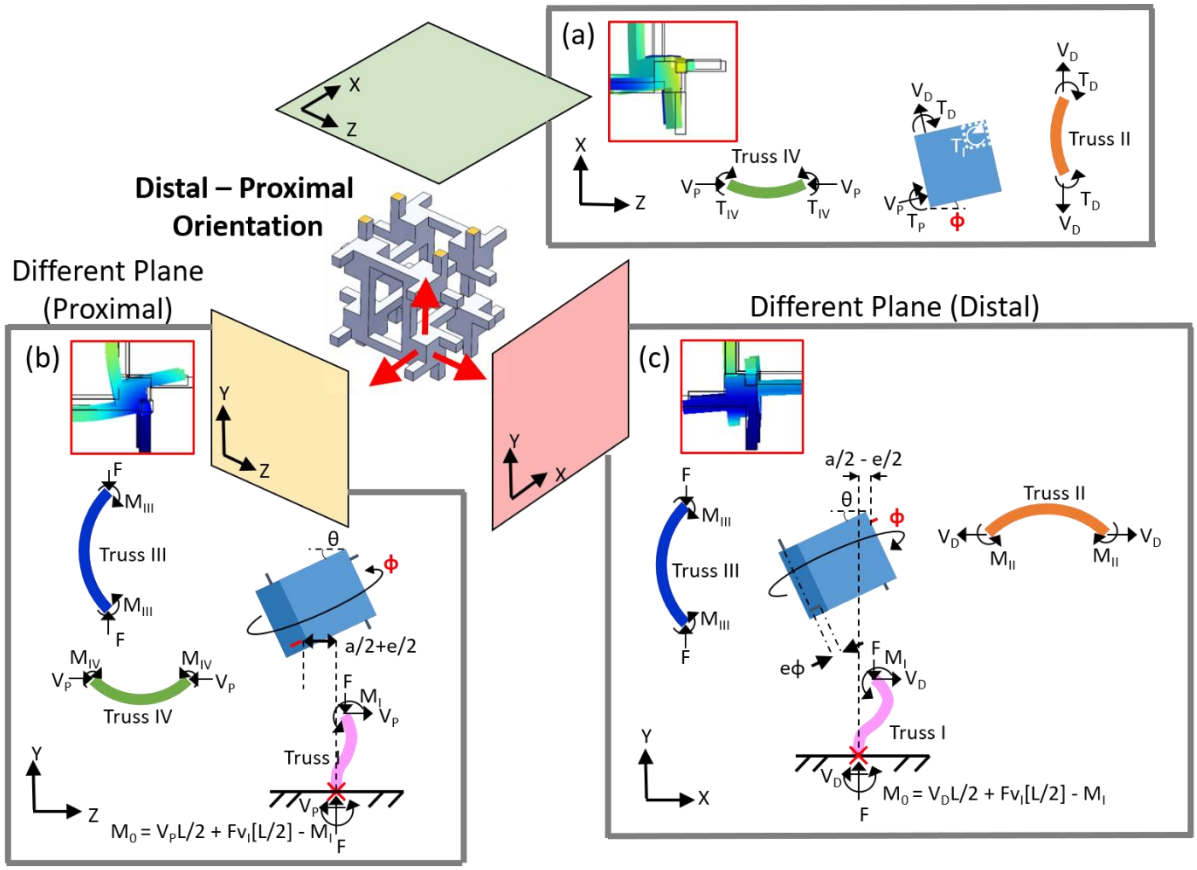

Figure A12: Free-body diagrams of the anti-tetrachiral unit-cell lattice, oriented in such a way that one load-bearing lateral truss is proximal, while the other is distal, to the clamped boundaries. The clamped boundaries are highlighted in yellow. The clamping is symmetrical, so the ends of the bottom-most vertical trusses are clamped as well. There are no constraints on the lateral sides of the lattice. The uniaxial load is applied vertically on the clamped surfaces. Because of symmetry, only the free-body diagrams for the bottom sub-unit cell (centre of the 3 red arrows) in different planes are shown. For simplicity, only load-bearing trusses are depicted. The point of origin for Truss I is marked by a red cross. The dashes at the perimeter of the central cubic joint indicate the positions where the trusses join with the cube. The red dash indicates the pivot of rotation *i.e.* the horizontal position of this point, at the end of the load-bearing lateral truss, is fixed. (a) Loading Plane: Top view showing the joint and the 2 lateral trusses, II and IV. (b) Transverse Plane 1: The boundary truss, Truss I, and the proximal lateral truss, Truss IV, are in parallel planes offset by a distance of e. (c) Transverse Plane 2: Truss I and the distal lateral truss, Truss II, are in parallel planes offset by a distance of *e*. θ is the in-plane rotation and may be different in (b) and (c). ϕ is the out-of-plane rotation that is the same in all planes. (Insets) Images from finite element simulations illustrating the deformation of the sub-unit cell in the respective planes.

A2.2. <u>Proximal Truss</u>

For the plane with the proximal truss (Fig. A2b), which is arbitrarily assigned Truss IV here, substituting ϕ from Eq. (A19) into Eq. (A12) gives

$$V_P = \frac{Q_P}{R_P + eF\xi} M_{I,P} + \frac{eF\xi}{R_P + eF\xi} V_D \quad \text{(A20)}$$

where

$$\xi = \frac{eL}{2E_s I}\left(\frac{1+\upsilon_s}{3+2\upsilon_s}\right) \quad \text{(A21)}$$

and

$$M_{I,P} = \frac{eF + C_{P1}}{C_{P0}}(V_P - V_D) \quad \text{(A22)}$$

where

$$C_{P0} = 2 + S + \frac{Q_P}{R_P}\left(\frac{a}{2} - \frac{e}{2} + U + N\right) \quad \text{(A23)}$$

$$C_{P1} = \left(\frac{\frac{a}{2} - \frac{e}{2} + U + N}{R_P}\right) eF\xi \quad \text{(A24)}$$

Note that V_z has been replaced with V_P here.

A2.3. <u>Distal Truss</u>

Similarly, for the plane with the distal truss, substituting ϕ in Eq. (A19) into Eq. (59) and solving gives

$$V_D = \frac{Q_D}{R_D + eF\xi} M_{I,D} + \frac{eF\xi}{R_D + eF\xi} V_P \quad \text{(A25)}$$

$$M_{I,D} = \frac{eF - C_{D1}}{C_{D0}}(V_P - V_D) \quad \text{(A26)}$$

where

$$C_{D0} = 2 + S + \frac{Q_D}{R_D}\left(\frac{a}{2} + \frac{e}{2} + U + N\right) \quad \text{(A27)}$$

$$C_{D1} = \left(\frac{\frac{a}{2} + \frac{e}{2} + U + N}{R_D}\right) eF\xi \quad \text{(A28)}$$

2.4. <u>Stress-Strain Relationship</u>

Solving Eq. (A20), (A22), (A25) and (A26) simultaneously gives

$$V_D = \frac{H_B + H_C}{H_A H_C - H_B H_D} eF \quad \text{(A29)*}$$

$$M_{I,D} = \frac{(R_P R_D + eF\xi R_D + eF\xi R_P)(H_B + H_C) - eF\xi Q_P (H_A + H_D)}{Q_D (R_P + eF\xi)(H_A H_C - H_B H_D)} eF \quad \text{(A30)*}$$

$$V_P = \frac{Q_P(H_A+H_D)+eF\xi(H_B+H_C)}{(R_P+eF\xi)(H_AH_C-H_BH_D)}eF \quad \text{(A31)*}$$

$$M_{I,P} = \frac{H_A+H_D}{H_AH_C-H_BH_D}eF \quad \text{(A32)*}$$

where

$$H_A = \frac{R_D}{Q_D}C_{D0}C_1' - \left(\frac{eF\xi}{R_P+eF\xi}-1\right)C_{D1} \quad \text{(A33)}$$

$$H_B = \frac{R_D}{Q_D}C_{D0}C_2' - \frac{C_{D1}Q_P}{R_P+eF\xi} \quad \text{(A34)}$$

$$H_C = C_{P0} - \frac{C_{P1}Q_P}{R_P+eF\xi} \quad \text{(A35)}$$

$$H_D = \left(\frac{eF\xi}{R_P+eF\xi}-1\right)C_{P1} \quad \text{(A36)}$$

and

$$C_1' = 1 + \frac{eF\xi}{R_D} - \frac{(eF\xi)^2}{R_D(R_P+eF\xi)} \quad \text{(A37)}$$

$$C_2' = \frac{eF\xi Q_P}{R_D(R_P+eF\xi)} \quad \text{(A38)}$$

Finally, by substituting Eq. (A29) and (A30), as well as Eq. (A31) and (A32), into Eq. (13), the rotation of the central cube in the plane with distal lateral truss, θ_D, and proximal truss, θ_P, can be found respectively. These rotations can then be substituted into Eq. (64) – (67) to obtain the stress-strain relationship for the ***D-P*** orientation.

Table A1: Geometric parameters of the 3ATC lattices subjected to finite element simulations. Dummy values for the material modulus, E_s = 1 GPa, and material Poisson's ratio, ν_s = 0.4, were used in the simulations, but they were of no consequence in the results as the lattice modulus would be normalized by E_s and variations in ν_s was not observed to change the elastic response of the lattices significantly (see Section "Dependence on Material Parameters").

Sample No.	a (mm)	e (mm)	w (mm)	L (mm)	ρ/ρ_s
1	3	0.667	1	20	0.00715
2				15	0.0123
3				10	0.0259
4				8	0.0383
5				6	0.0617
6				4	0.114
7				3.2	0.154
8				2.6	0.198
9				2	0.264
10		1.33		20	0.00715
11				15	0.0123
12				10	0.0259
13				8	0.0383
14				6	0.0617
15				4	0.114
16				3.2	0.154
17				2.6	0.198
18				2	0.264
19		2		20	0.00715
20				15	0.0123

21				10	0.0259
22				8	0.0383
23				6	0.0617
24				4	0.114
25				3.2	0.154
26				2.6	0.198
27				2	0.264
28	4	2	0.5	4	0.131
29			1.0		0.148
30			1.5		0.178
31			2.0		0.219
32			0.5	6	0.0685
33			1.0		0.0820
34			1.5		0.105
35			2.0		0.136
36			0.5	10	0.0261
37			1.0		0.0343
38			1.5		0.0479
39			2.0		0.0671